An Cretaceous carbonate replacement origin for the Xinqiao stratabound massive sulfide deposit, Middle-Lower Yangtze Metallogenic Belt, China

Yang Li[1, 2 †], Jian-Wei Li[1], Xian-Hua Li[3], David Selby[2], Guang-Huan Huang[1], Lin-Jie Chen[4] and Kai Zheng[4]

[1] Faculty of Earth Resources, China University of Geosciences, Wuhan, 430074, China

[2]Department of Earth Sciences, Durham University, Durham, DH1 3LE, UK

[3]State Key Laboratory of Lithospheric Evolution, Institute of Geology and Geophysics, Chinese Academy of Sciences, Beijing, 100029, China

[4]321 Geological Team, Bureau of Geology and Mineral Exploration of Anhui province, Tongling, 244033, China

[†] Corresponding author Email, li.yang@durham.ac.uk, cugliyang@126.com

Abstract

Stratabound massive sulfide deposits are widespread along the Middle-Lower Yangtze Metallogenic Belt (MLYMB) and serve as an important copper producer in China. Two contrasting genetic models have been proposed, interpreting the stratabound massive sulfide deposits as a Carboniferous SEDEX protore overprinted by Cretaceous magmatic-hydrothermal system or an Early Cretaceous carbonate replacement deposit. These two contrasting models have been applied to the Xinqiao stratabound Cu-Au sulfide deposit, which is dominated by massive sulfide ores hosted in marine carbonates of the Carboniferous Chuanshan and Huanglong Formations, with minor Cu-Au skarn ores localized in the contact zone between the Cretaceous diorite Jitou stock and the Carboniferous carbonate rocks. New SIMS zircon U-Pb dating suggests that the Jitou stock formed at 138.5 ± 1.1 Ma (2σ, MSWD = 0.6), whereas an unaltered diorite porphyry dike in the mine was emplaced at 130.6 ± 1.1 Ma (2σ, MSWD = 0.1). Pyrite Re-Os dating yields an imprecise date of 142 ± 47 Ma (2σ, MSWD = 7.8). The geochronological data thus constrain the mineralization of the Xinqiao deposit as early Cretaceous.

Fluid inclusions in prograde skarn diopside have homogenization temperatures of 450-600 ^{o}C and calculated salinities of 13-58 wt. % NaCl equiv. Quartz from the stratabound ores and pyrite-quartz vein networks beneath the stratabound ores have homogenization temperatures of 290-360 and 200-300 ^{o}C, with calculated salinities of 5-12 and 2-10 wt. % NaCl equiv., respectively. Quartz from the skarn ores and veins beneath the stratabound ores have δ^{18}O values of 12.32 ± 0.55 (2 SD, n = 22) and 15.57 ± 1.92 ‰ (2 SD, n = 60), respectively, corresponding to calculated δ^{18}Ovalues of 6.22 ± 1.59 (2σ) and 6.81 ± 2.76 ‰ (2σ) for the equilibrated ore-forming fluids. The fluid inclusion and oxygen isotope data thus support a magmatic-

hydrothermal origin rather than a SEDEX system for the stratabound ores, with the hydrothermal fluids most likely being derived from the Jitou stock or associated concealed intrusion. Results from this study have broad implications for the genesis and exploration of other stratabound massive sulfide deposits along the MLYMB.

Keywords

Stratabound Massive Sulfide Deposit, SIMS Oxygen Isotope, Zircon U-Pb, Pyrite Re-Os, Fluid Inclusion, Carbonate Replacement Deposit

Introduction

Stratabound massive sulfide deposits have been well documented in Mexico (Meinert 1982) and north-central Chile (Sato 1984), which have been commonly considered as carbonate replacement deposits (CRD). Equivalents of this type of deposits are widespread along the Middle-Lower Yangtze Metallogenic Belt (MLYMB), having been important copper producers in China during the last three decades (e.g., Pan and Dong 1999; Mao et al. 2011 and references therein). These deposits are predominantly hosted in Carboniferous carbonates, but show a close spatial association with Cretaceous granitoid intrusions that are genetically related to porphyry-skarn ores (Mao et al. 2011 and references therein). Despite many years of research, considerable debate remains on the genesis of these deposits (Guo et al. 2011; Mao et al. 2011; Xie et al. 2014; Xiao et al. 2016). Several studies advocate that the stratabound massive sulfide deposits are products of a Carboniferous sedimentary exhalative (SEDEX) system, which was overprinted by hydrothermal fluids associated with Cretaceous magmatism (Gu et al. 2000; Gu et al. 2007; Zhou et al. 2010; Guo et al. 2011; Xie et al. 2014; Xiao et al. 2016). In contrast, some authors considered these deposits as skarn/carbonate replacement systems genetically associated with Cretaceous magmatism (Pan and Dong 1999; Mao et al. 2011; Zhang et al. 2015). The contrasting genetic models have hampered recent mineral exploration strategies (Guo et al. 2011; Mao et al. 2011; Xie et al. 2014; Xiao et al. 2016).

The Wushan and Chengmenshan deposits in the Jiurui district, west MLYMB, and Dongguashan and Xinqiao deposits in the Tongling district, central MLYMB (Fig. 1) are the most important and representative stratabound massive sulfide deposits within this giant metallogenic belt. In these mining districts, stratabound orebodies are mostly hosted in Late Carboniferous limestone and dolomite and, to a lesser extent, in the Early Permian limestone. In

addition to the stratabound occurrence, the stratabound orebodies are characterized by laminated structures and local presence of colloform pyrite. Another striking feature is the development of vertical to sub-vertical pyrite-quartz vein networks beneath stratabound orebodies. These field observations indicate that Xinqiao deposit share many similarities with typical SEDEX deposits (Large 1983; Leach et al. 2004; Leach et al. 2005). On the other hand, most of the stratabound deposits show close spatial association with Cretaceous intrusions that also exhibit variable amounts of porphyry-skarn mineralization (Pan and Dong 1999; Gu et al. 2007; Mao et al. 2011). Coexistence of SEDEX textures and magmatic association has resulted in a prolonged debate about the genesis of those stratabound massive sulfide deposits (Pan and Dong 1999; Gu et al. 2007; Zhou et al. 2008; Guo et al. 2011; Mao et al. 2011; Xie et al. 2014; Zhang et al. 2015; Xiao et al. 2016).

In this paper, we present fluid inclusion, quartz oxygen isotope, zircon U-Pb and pyrite Re-Os data for the Xinqiao stratabound massive sulfide deposit. These new data are used to constrain the nature and origin of ore-forming fluids, emplacement age of the Cretaceous intrusions, and ultimately ore genesis. Combined with published geochemical and geochronological data, results from this study suggest a Cretaceous magmatic origin for the Xinqiao deposit. Our study also has implications for genesis of other stratabound massive sulfide deposits along MLYMB, and may offer guidance for future exploration within this metallogenic belt.

Geologic background

The MLYMB is located along the NE margin of the Yangtze craton that is separated from the Dabie Ultra-High Pressure Belt (UHP) by the Xiangfan-Guangji Fault in the north, and from

93 the North China craton by the Tancheng-Lujiang (Tan-Lu) Fault in the northeast (Fig. 1). The
94 Changzhou-Yangxin and Guangde Faults define the southern and eastern boundaries of the
95 MLYMB, respectively (Pan and Dong 1999).The northern Yangtze craton is underlain by
96 tonalitic-trondjhemitic-granitic (TTG) gneisses and amphibolite to granulite facies supracrustal
97 rocks (Zhao et al. 2011; Wan 2012). The TTG rocks have LA-ICP-MS zircon U-Pb ages ranging
98 from 3.45 to 2.87 Ga (Guo et al. 2014). The TTG dominated basement rocks are unconformably
99 overlain by Late Archean to Paleoproterozoic (2900-1895 Ma) calc-alkaline basalts, rhyolites,
100 carbonate and clastic sedimentary rocks that metamorphosed to amphibolite and granulite facies
101 (Pan and Dong 1999). Continent-rifting or subduction related magmatism occurred at 848 ± 4
102 Ma (Li et al. 2008). Caron-wide marine deposition occurred from the Cambrian to the Late
103 Devonian and ceased during the Early Carboniferous as a result of uplift of the Yangtze craton
104 (Pan and Dong 1999; Wan 2012). Subsidence of the Yangtze craton during the Late
105 Carboniferous permitted further marine sedimentation until the Late Triassic (Wu et al. 2003;
106 Wan 2012). The Proterozoic to Triassic strata have been pervasively affected by the Triassic
107 Indosinian Orogeny involving the continental collision between the Indochina and South China
108 blocks (Wu et al. 2003; Wan 2012).
109 Within the MLYMB, Late Silurian sandstones are unconformably overlain by sandstones of
110 the Late Devonian Wutong Formation, which are unconformably overlain by sandstones of Early
111 Carboniferous Gaolishan Formation. The Late Carboniferous Huanglong Formation dolomites
112 and limestones are paraconformable lying above the Gaolishan Formation. Above the Huanglong
113 Formation is Late Carboniferous Chuanshan Formation limestone. Paraconformably overlying
114 the Chuanshan Formation is the Early Permian Qixia Formation, which comprises carbonaceous
115 shales, siltstones and intercalated mudstones, carbonaceous limestone. Middle to Upper Permian

Maokou, Longtan and Dalong Formations are dominated by cherts, shales, calcareous shales, banded limestone, and layered limestone. The latter formations are overlain by Triassic sediments that are dominated by limestone, dolomite, clastic rocks (sandstone) and shales (Pan and Dong 1999).

Granitoid intrusions and volcanic rocks are widely distributed throughout the MLYMB (Fig. 1). These magmatic units are divided into two groups based on their formation ages and lithologies (Zhou et al. 2008; Mao et al. 2011). The first group is dominated by granitoid intrusions emplaced between 148 and 135 Ma, and is widely distributed in Daye, Jiurui, Anqing, Tongling and Ningzhen districts (Fig. 1). The second group is composed of volcanic and subvolcanic rocks formed between133 and 123 Ma, which are mostly distributed in Ningwu and Luzong volcanic basins (Fig. 1). Group one intrusions are dominated by quartz diorite, granodiorite, and monzonite, with subordinate gabbro, diorite, syenite and granite, and are associated with the majority of Cu-Au and Cu-Fe porphyry-skarn deposits throughout MLYMB (Zhou et al. 2008; Mao et al. 2011). In contrast, the second group volcanic-subvolcanic sequences are spatially and temporally related to the skarn and Kiruna-type iron deposits (Zhou et al. 2008; Mao et al. 2011).

A thrust fault is recognised broadly along the unconformity between Late Devonian sandstone and Early Carboniferous carbonates, which formed during the Triassic Indosinian Orogeny, and was reactivated during the Late Mesozoic Yanshan Orogeny associated with westward subduction of the paleo-Pacific plate (Li and Fu 1991; Wu et al. 2003; Li and Li 2007). This thrust system and its associated structures have a close spatial association with the Cretaceous intrusions and resultant porphyry-skarn Fe-Cu mineralization. In addition, almost all

138 the stratabound massive sulfide deposits in MLYMB occur along the thrust system (Wu et al.
139 2003).
140
141 **Geology of the Xinqiao deposit**
142 **Stratigraphy**
143 The stratigraphic column of sedimentary rocks exposed in the Xinqiao mine and surrounding
144 areas is presented in Fig. 2 (803-Geological-Team 1971). The oldest rocks exposed are the
145 Silurian sandstone and shales, which are unconformably overlain by the Late Devonian Wutong
146 Formation. The Wutong Formation consists of pale-yellow quartz sandstone of 140 m thickness,
147 with interbedded dark-grey shale and sandy shale. Quartz conglomerate with a thickness of 10-
148 30 cm is present at the top of the Wutong Formation in the mining area (803-Geological-Team
149 1971).
150 The Early Carboniferous Gaolishan Formation has a thickness of 30-50 m and is
151 paraconformable with the underlying Wutong Formation. The lower and middle Gaolishan
152 Formation predominately consists of pale-yellow and pale quartz sandstone, while the upper part
153 comprises fine-grained quartz conglomerate, siltstone, and silty shales. The upper part of the
154 Gaolishan Formation is extensively fractured (Li and Fu 1991) and contains abundant pyrite-
155 quartz veins with a volume percentage of 5-25, which represent the main host of Au at Xinqiao
156 (803-Geological-Team 1971). Pyrite grains are generally euhedral or subeuhedral cubic crystals
157 with a grain-size of 0.5-1 mm, but 2-5 mm grains are also documented (Guo et al. 2011).
158 Overlying the Gaolishan Formation is the Late Carboniferous Huanglong Formation which
159 includes ~30 m of limestone, dolomitic limestone and dolomite with locally presented silty
160 sandstone at the base of the formation. The main stratabound massive sulfide orebody is hosted

within the bottom part of the Huanglong Formation and above the Gaolishan Formation (Fig. 3; 803-Geological-Team 1971). Consequently, the bottom part of the Huanglong Formation is significantly replaced by the massive sulfide orebody, and in certain cases is completely replaced, as best illustrated near the Cretaceous Jitou stock (Fig. 3B and C).

The Late Carboniferous Chuanshan Formation is 60 m thick. The lower part of the Chuanshan Formation is dominated by limestone in paraconformable contact with the underlying Huanglong Formation. The upper part of the Chuanshan Formation comprises laminated limestone and fossiliferous clastic limestone.

Paracomformably overlying the Chuanshan Formation is the Early Permian Qixia Formation, which is composed of dark-grey carbonaceous limestone and grey cherty or nodular cherty limestone in the lower and upper parts, respectively.

Permian-Triassic limestone, calcareous shale, cherty shale, silty shale and sandstone are widely distributed in the mining area with a total thickness of > 350 m.

All the carbonates in the mining area experienced variable degrees of metamorphism associated with the emplacement of the Cretaceous intrusions discussed below (803-Geological-Team 1971). Siltstone and silty shales of the Gaolishan Formation, which serves as the footwall of the massive orebody, exhibit extensive sericitization, with locally distributed hornfels (803-Geological-Team 1971; Xu and Zhou 2001). The thrust system in Xinqiao mining area is broadly parallel to the unconformity between the Gaolishan and Huanglong Formations, and in some cases Chuanshan Formation carbonates are also part of this thrust system. Fault breccias are composed of limestone and silty shales, which have been thermally metamorphosed to marble and hornfels (803-Geological-Team 1971; Li and Fu 1991; Wu et al. 2003).

184 **Igneous rocks**

185 Magmatism in the Xinqiao mine is largely represented by the Cretaceous Jitou quartz diorite
186 stock (Figs. 6A, B), with additional dikes and sills of similar compositions (Fig. 3; 803-
187 Geological-Team 1971; Xu and Zhou 2001).

188 The Jitou stock intrudes the Permian-Triassic carbonates and has an outcrop of 0.3 km^2 (Fig.
189 3A). Drill-core logging indicate it extends northward at depth (Fig. 3B; 803-Geological-Team
190 1971). Though there is no obviously compositional variations across the pluton, but can be
191 divided into a medium-grained central phase and a porphyritic marginal phase. The central phase
192 (Fig. 3A) is dominated by quartz diorite (Fig. 6A) comprising plagioclase (60 vol. %), quartz (25
193 vol. %) and hornblende (9 vol. %) with minor alkali feldspar (4 vol. %) and biotite (1 vol. %),
194 and accessory minerals including zircon, titanite, apatite and magnetite. The marginal phase is
195 dominated by diorite porphyry (Fig. 6B) which comprises plagioclase (30 vol. %) and
196 hornblende (20 vol. %) as phenocrysts, and groundmass dominated by plagioclase (25 vol. %),
197 quartz (20 vol. %) and hornblende (2 vol. %), and accessory minerals that include apatite, titanite,
198 zircon and magnetite. In addition, monzonite is also documented as a component of the marginal
199 phase (Wu et al. 2009).

200 Several quartz diorite and porphyritic diorite dikes and sills are exposed or revealed via drill
201 cores. The dikes and sills are compositionally and texturally similar to the marginal phase of the
202 Jitou stock. The dikes and sills are particularly abundant in the northeast side of the Jitou stock
203 (Fig. 3B), in the hanging-wall of the Qixia Formation, and along stratigraphic contacts. It is
204 thought the Jitou stock provided a feeder for these dikes and sills (803-Geological-Team 1971).
205 These dikes and sills, and the marginal phase of the Jitou stock as well, exhibit extensive
206 alteration (see below), as indicated by feldspar dissolution (Fig. 6B).

A diorite porphyry dike was encountered during the mining activity in the southeast wall of the open pit (Fig. 6C). This dyke consists of plagioclase (27 vol. %) and hornblende (8 vol. %) as phenocrysts, with a groundmass predominately comprising plagioclase (48 vol. %) and quartz (15 vol. %), and accessory minerals that include pyrite, magnetite, apatite and zircon. No associated mineralization or alteration has been documented for this dike.

Mineralization and alteration

The Xinqiao deposit has an estimated resource of 10.22 million tonnes at an average of 0.938 % Cu and 34.87 % S, respectively. Greater than 90 % of the resource is hosted by the main stratabound-type orebody that is located along the lithological contact of Gaolishan and Huanglong Formations (Fig. 3; 803-Geological-Team 1971). It extends along a NE-strike for 2.56 km and average 21 m in thickness, with the thickest segments (~70 m) occurring in close proximity to the Jitou stock (Fig. 3; 803-Geological-Team 1971). Minor massive orebodies are fault hosted (Fig. 3B). The Xinqiao deposit average at 0.73 g/t Au,14.12 g/t Ag, and 0.5 % Zn, but the supergene zones, which has been mined out, contained up to 2 g/t Au and 70g/t Ag. The ore grades of the stratabound orebody appear to be spatially associated with the Jitou stock, with the highest Cu, S, Au, and Ag being present in proximity of the Jitou stock (Fig. 5A; 803-Geological-Team 1971). The Xinqiao deposit is characterized by metal and ore zonation (Fig. 5B). From the intrusive contact of the Jitou intrusion towards the Carbonaceous strata, the ores are dominated by magnetite, chalcopyrite, pyrite, and Zn-Pb sulfides (Fig. 5B). Mineralization and alteration associations, revealed from bench mapping, core logging and petrographic analysis, are presented in Figures 6-7, with the ore paragenesis summarized in Figure 8.

Skarn assemblages, although volumetrically minor, represent the most intensive alteration at Xinqiao (Fig. 3B, C). The skarn alteration is largely restricted within the contact zone between the Jitou stock and the Permian Qixia Formation limestone (Fig. 3C), but also extends locally into the stratabound orebody distal to the intrusion (Fig. 3B). The skarn alteration typically contains brown to dark-red, anhedral garnet (Fig. 6D), which is commonly overprinted by minor retrograde assemblage, which include actinolite, phlogopite, chlorite, epidote, and tremolite. Wollastonite clusters associated with garnet and diopside assemblages (Fig. 6E) are also developed within the Jitou stock, as a result of hydrothermal metasomatism of carbonate xenoliths (Fig. 3B, C). Epidote also occurs near the intrusive contact zone (Fig. 6F). Late stage euhedral calcite (grain size of ~1-3 cm) occurs in the garnet skarn and are typically enveloped by 1-5 cm wide hematite rings (Fig. 6D). Hydrothermal alteration, largely represented by feldspar dissolution (Fig. 6B) and chlorite formation (Fig. 3G), is extensive throughout the marginal phase of the Jitou stock.

Hydrothermal alteration is relatively weak on both the footwall and hanging walls of the stratabound massive sulfide orebody (803-Geological-Team 1971; Xu and Zhou 2001). However, silicification is variably developed in the sandstones of the Gaolishan Formation, and is generally associated with sericitization whenever silicate clasts are present in the sandstones. The silicification tends to be more intensive close to the stratabound orebody and where sandstones are extensively fractured (Fig. 6O).

Below the stratabound orebody and within the silicificated Gaolishan Formation sandstone, there are numerous planar or wavy quartz vein networks (Gu et al. 2000; Guo et al. 2011), which have been previously interpreted to represent fluid conduits of a submarine exhalative system. The veins comprise subeuhedral-anhedral pyrite grains ranging in size from 0.5to 2 cm and

252 anhedral fine-grained (<0.3 mm) quartz. In places the vein networks are perpendicular to the
253 stratabound orebody. The pyrite-quartz veins have a sharp contact with the sandstones and lack
254 extensive hydrothermal alteration halos on both sides of the veins except for narrow (commonly
255 <0.5 cm wide) silicification and sericitization selvages.

256 In the hanging wall of the Qixia Formation limestone, pyrite veins, which are tens of
257 centimetres to meters wide, are locally abundant (Fig. 4). These veins are typically associated
258 with meter-wide marble zones, but no obvious alteration assemblages are documented (803-
259 Geological-Team 1971).

260 Magnetite is the dominant ore mineral in skarn mineralization, comprising 50-60 vol % of
261 the bulk skarn ore (Fig. 6H). The magnetite ore generally has a massive texture. Although
262 chalcopyrite occurs as centimetre-sized clusters and several millimetre wide veins, it is only sub-
263 economic in the skarn mineralization (803-Geological-Team 1971). Typical pyrite mineralization
264 in the skarn ore occurs as subparallel pyrite veins in quartz dominated matrix with banded
265 textures (Fig. 6I). Skarn hosted pyrite are generally anhedral with a grain size of ~0.3-2 cm
266 associated with anhedral fine-grained (<0.5 cm) quartz.

267 The stratabound sulfide orebody in the Xinqiao deposit is dominated by massive pyrite ore
268 (Fig. 6J-L), although massive chalcopyrite and sphalerite veins are also present (Fig. 6M-N).
269 Three types of pyrite have been identified (py1, py2 and py3). In addition, previous studies
270 document pentagonal, dodecahedron and fine-grained anhedral pyrite (Zhou et al. 2010; Xiao et
271 al. 2016). Type 1 pyrite (py1) is the most abundant and consists of anhedral grains with micro-
272 fractures (Fig. 6J, 7B). It typically occurs without associated minerals, with rare exceptions
273 where quartz and chalcopyrite veinlets are observed. Type 2 pyrite is euhedral with a cubic form,
274 and typically occurs as clusters with a grain size of 0.3-2.5 cm (Fig. 6K, 7A), and is not

associated with other minerals. Type 3 is featured by massive colloform texture (Fig. 6L). The colloform pyrite has zoned texture (Fig. 7C) with individual grains ranging from 0.5 to 2 μm size (Zhou et al. 2010; Xie et al. 2014; Xiao et al. 2016). In places, the colloform pyrite includes silver-yellow anhedral pyrite clusters, and is cut by ~0.5 cm wide silver-yellow pyrite veins (Fig. 6L).

Massive chalcopyrite is also present in the stratabound orebody. Chalcopyrite ore typically has a green-yellow colour with massive texture and is predominately comprised of chalcopyrite (Fig. 6M). Sphalerite occurs as 5-10 cm wide veins in the Qixia Formation limestone, with associated calcite and pyrite (Fig. 6N). In addition, sphalerite is also present as solid solution in chalcopyrite (803-Geological-Team 1971).

Samples and Analytical methods

Samples

Two diopside-bearing samples (XQ7 and XQ10; Fig. 6E) were collected from the contact zone (Fig. 3B) between the Jitou stock and the Qixia Formation dolomitic limestone in the open pit. Two quartz bearing banded pyrite-quartz vein (Fig. 6I) samples (XQ82 and XQ86) were collected from the same position. A further two quartz bearing samples (XQ8-1 and XQ8-2) were collected from the Gaolishan Formation sandstone hosting quartz-pyrite vein networks (Fig. 6O) at the north wall of the open pit (Fig. 3B). Diopside and quartz bearing assemblages from these samples were selected for fluid inclusion study.

Samples (XQ5-1, 5-2 and 5-3) used for SIMS oxygen isotope analysis also were collected from the contact zone (Fig. 3B) between the Jitou stock and the Qixia Formation dolomitic limestone in the open pit. These samples are dominated by anhedral garnet overprinted with

298 calcite (Fig. 6D) and anhedral quartz interstitial to the garnet grains (Fig. 7E). Four quartz-pyrite
299 veins (XQ8-3, 8-4, 8-5 and 8-6) hosted in the Gaolishan Formation sandstone were collected
300 from the same position as XQ8-1 and 8-2.

301 One diorite porphyry sample (XQ09-3) was collected from the marginal phase of the Jitou
302 stock (Fig. 3B), and comprises plagioclase (27 vol. %) and hornblende (23 vol. %) as
303 phenocrysts, with a groundmass of plagioclase, quartz and hornblende, and accessory minerals of
304 apatite, titanite, zircon and magnetite. The sample possesses extensive plagioclase phenocryst
305 dissolution indicating intensive hydrothermal alteration (Fig. 6B). The XQ1 sample was
306 collected from south wall of the open pit (Fig. 3B), which is diorite porphyry in composition.
307 This unit has a similar mineralogy to the marginal phase of the Jitou stock, but possesses less
308 abundant phenocrysts and is free of alteration (Fig. 6C). Zircon grains were separated from these
309 two samples for SIMS U-Pb geochronology.

310 Four massive pyrite samples were collected from the main stratabound massive sulfide
311 orebody at the bottom northeast corner of the open pit for Re-Os geochronology study. Samples
312 XQ15 and XQ24 are dominated by py1 (Fig. 6J, 7B), whereas samples XQ25 and XQ10 are
313 mainly composed of py2 (Fig. 6K, 7A)..

314

315 **Microthermometry**

316 Microthermometric analysis of fluid inclusions in diopside and quartz was carried out at the
317 fluid inclusion laboratory at the Faculty of Earth Resources, China University of Geosciences,
318 Wuhan, using a Linkam THMS600 heating and freezing stage mounted on an Olympus
319 transmission light microscope. Synthetic fluid inclusion standards (pure CO_2 and pure water)
320 were used at -56.6, 0, 10.2, and 374°C to assess the accuracy of the stage (Baumgartner et al.

2014). Analytical uncertainties are better than ±0.2 °C and ± 1 °C for measurements below and above 31.1 °C (critical point of CO_2), respectively. The volumetric fraction of liquid or vapor phases present in fluid inclusions was estimated at room temperature with reference to the volumetric chart of Roedder (1984). Bulk salinity was calculated from the final ice melting temperature, or halite dissolution temperature (Bodnar and Vityk 1994) for hypersaline fluid inclusions.

SIMS oxygen isotope analysis

Quartz oxygen isotope analysis was carried out at the Institute of Geology and Geophysics, Chinese Academy of Sciences with a CAMECA IMS-1280 SIMS. Sample preparation and instrument operation conditions are the same as Li et al. (2010a) and are briefly summarized here. Quartz bearing assemblages were mounted with NBS-28 (Matsuhisa 1974) and Qinghu quartz standards and then polished and coated with gold. The Cs^+ primary ion beam was accelerated at 10 kV, with a beam intensity of ca. 2 nA and rastered over a 10 μm area. The spot size as an ellipse was about 10 × 20 μm in diameter. Oxygen isotopes were measured using multi-collection mode on two off-axis Faraday cups. The intensity of ^{16}O ion was typically 10^9 cps during this study. The instrumental mass fractionation factor (IMF) was corrected using NBS-28 with a $\delta^{18}O$ value of 9.5 ‰ (V-SMOW, same as below; Matsuhisa 1974). Measured $^{18}O/^{16}O$ ratios were normalized by using V-SMOW compositions ($^{18}O/^{16}O$ = 0.0020052), and then corrected for the IMF. Uncertainties on individual analysis were usually better than 0.3 ‰ (2 SE). All measurements were bracketed by or interspersed with analyses of Qinghu quartz that served as an in-house standards. Our measurements of Qinghu quartz showed small amounts of random drift through time (in all cases <0.6 ‰). The weighted mean of 41 measurements is 8.66 ± 0.05 ‰

(95 % conf., Table A1, Fig. A1, 2 SD = 0.28), which is identical, within uncertainty, to the recommended value (8.6 ± 0.2 ‰; 2 SD, Li Xian-Hua, unpublished). The data are reported in Table 1 and graphically presented in Fig.10. The weighted mean $\delta^{18}O$ value of each sample was calculated by *Isoplot 3.0* with rejection of any data outside of the 2 sigma uncertainty (Ludwig 2003).

SIMS zircon U-Pb dating

Zircon U-Pb dating was conducted at the Institute of Geology and Geophysics, Chinese Academy of Sciences with a CAMECA IMS-1280HR SIMS. Sample preparation and instrument operation conditions are the same as previous studies (Li et al. 2009; Li et al. 2010a) and are briefly summarized here.

Zircon grains were mounted with geochronology standards (Plešovice and Qinghu zircon) (Sláma et al. 2008; Li et al. 2013) and then polished and coated with gold. During U-Pb analysis, zircon grains were sputtered by an O^{2-} primary ion beam with a beam intensity of ca. 8 nA and a beam diameter of 20 μm. An ellipsoidal spot approximately 20 × 30 μm in size was created at the sample surface as the ion beam was at an angle with the sample surface. U-Pb concentration and isotopic compositions were calibrated against the Plešovice zircon standard with a recommended age of 337.13 ± 0.37 Ma (Sláma et al. 2008). Common Pb was corrected using measured non-radiogenic ^{204}Pb and an average present day crustal Pb isotopic composition defined by Stacey and Kramers (1975). The Wetherill concordia plots and derived concordia ages were calculated by using *Isoplot* v.3.0 (Ludwig 2003). As a monitor of data quality, the Qinghu zircon standard was analysed between samples. Seven analyses of Qinghu zircon during this study (Table A2, Fig. A2) yielded a weighted mean $^{206}Pb/^{238}U$ age of 160.1 ± 1.8 Ma at 95 % confidence (MSWD

= 0.43), which is in agreement with the reported reference value of 159.5 ± 0.2 Ma (Li et al. 2013). The U-Pb data are reported in Table 2, and illustrated in Wetherill concordia plots and weighted average of $^{206}Pb/^{238}U$ ages (Fig.11).

Pyrite Re-Os dating

Massive pyrite samples were crushed to 20-30 mesh and then handpicked under a microscope, the estimated pyrite purity is better than 98 %. The pyrite Re-Os analytical method was the same as documented by Selby et al. (2009) and is briefly outlined here. Purified pyrite aliquots were accurately weighted and loaded into carius tubes with known amounts of mixed Re-Os tracer solution containing ^{185}Re and ^{190}Os. The carius tubes were then sealed, digested and equilibrated using a mix of 11 N HCl (3 ml) and 15.5 N HNO_3 (8 ml) at 220 ^{o}C for 48 hours. Osmium was isolated and purified from the acidic digestion medium using solvent ($CHCl_3$) and microdistillation methods, and rhenium was separated by solvent extraction (acetone) and anion chromatography (Selby and Creaser 2001). The purified Re and Os were loaded onto Ni and Pt filaments, respectively, with the isotopic measurements conducted using negative thermal ionization mass spectrometry (Creaser et al. 1991) on a Thermo Electron TRITON mass spectrometer. The Os data was collected via ion counting using a secondary electron multiplier in peak-hopping mode, and Re data was collected with static Faraday collectors. Total procedural blanks were monitored during the course of study. Blanks for Re and Os were 2.8 ± 0.6 and 1.7 ± 2.0 pg, respectively, with an average $^{187}Os/^{188}Os$ value of 0.19 ± 0.10 (2σ, n = 3). The presented uncertainties include the fully propagated uncertainties in Re and Os isotopic compositions measurements, blank abundances and isotopic compositions, spike calibrations and

reproducibility of standard Re and Os isotope values. Decay constant uncertainties are not propagated as the uncertainty of Re-Os is dominated by analytical uncertainty.

Results

Fluid inclusion

Fluid inclusions were classified as primary, pseudosecondary and secondary inclusions following the definition of Goldstein and Reynolds (1994). Both primary and pseudosecondary fluid inclusions homogenised to liquid followed by dissolution of halite whenever it is present. No clathrate formation was recorded in this study. However, a few fluid inclusions hosted in diopside, 6 of them did not homogenize despite heating to ~598 ºC for ~10 minutes.

Diopside predominately hosts liquid-vapor two-phase fluid inclusions with a few containing halite as daughter minerals. These fluid inclusions are generally round and vary in size from 5 to 12 μm (Fig. 9A&B). Vapor phase accounts for 30 and 60 vol. % of individual fluid inclusions. Thirty-nine measurements yield variable homogenization temperatures and calculated salinities (Fig. 10). The two-phase aqueous fluid inclusions (n = 28) yielded homogenization temperatures of 450-~600 ºC and calculated salinities of 13-21 wt. % NaCl equiv. The halite bearing inclusions (n = 11) yield homogenization temperatures of 450 to ~600 ºC and salinities of 35-58 wt. % NaCl equiv. calculated from halite melting temperature

Quartz from the banded quartz-pyrite veins in the skarn ores hosts abundant two-phase aqueous fluid inclusions, which are round to sub-round or polygonal in shape, range in size from a few to >10 μm, and contain 20-50 vol. % vapor phase (Fig. 9C). Homogenization temperatures and calculated salinities for these fluid inclusions (n = 29) are 290-360 ºC (average = 328 ± 46 ˚C), and 5-12 wt. % NaCl equiv, respectively (Fig. 10).

412 Quartz from the quartz-pyrite vein networks in the Gaolishan Formation sandstone host
413 liquid-rich aqueous fluid inclusions that are elongated with a diameter of ~10 μm and contain
414 <35 vol. % vapor. The inclusions (n = 46) yielded homogenization temperatures between 200
415 and 300 ºC (average = 258 ± 42 ˚C), and calculated salinities of 2-10 wt. % NaCl equiv. (Fig. 10).
416
417 **Oxygen isotopes**
418 In total, 32 and 71 *in-situ* quartz oxygen isotope analyses were conducted for quartz from the
419 banded skarn ore (Fig. 6I, 7E) and quartz-pyrite veins in the Gaolishan Formation sandstone (Fig.
420 6O, 7F), respectively. Mineral inclusions are rare in these anhedral quartz grains except pyrite in
421 some cases (Fig. 7E-F). The analysed quartz grains exhibit no cathodoluminescence, indicating
422 homogeneous texture and composition. The data are reported in Table 1 and graphically
423 presented in Figure 11.
424 Quartz grains from the skarn ore samples yield $\delta^{18}O$ values of 11.09 to 13.79 ‰ (2 SD; n =
425 22). No systematic variation in the $\delta^{18}O$ values were observed between samples. Quartz from
426 quartz-pyrite vein networks in the Gaolishan Formation sandstone yield $\delta^{18}O$ values
427 predominately between 13.47 and 17.76 ‰, with a mean of 15.57 ± 1.92 (2 SD, n = 60). Again,
428 no systematic $\delta^{18}O$ values variations were observed among the analysed samples.
429
430 **Zircon U-Pb ages**
431 All zircon grains recovered from the marginal phase of the Jitou stock and the alteration-free
432 diorite porphyry dike are pale, euhedral and prismatic, and their CL images revealed well-
433 developed oscillatory zonation (Fig. 12). The morphological and textural features confirm a
434 magmatic origin for the zircon grains investigated. The U-Pb data are summarized in Table 2 and

illustrated in Figure 12. For the marginal phase diorite porphyry of the Jitou stock, 16 analyses yield a Wetherill concordia age of 138.5 ± 1.0 Ma (95 % conf., MSWD = 0.6), which is identical to the weighted mean $^{206}Pb/^{238}U$ age (138.5 ± 1.0 Ma, 95 % conf., MSWD = 0.24). For the diorite porphyry dike, 22 analyses showed limited scatter and yield a Wetherill concordia age of 130.6 ± 1.1 Ma (95 % conf., MSWD = 0.1), and an identical weighted average of $^{206}Pb/^{238}U$ age of 130.7 ± 0.9 Ma (95 % conf., MSWD = 1.1).

Pyrite Re-Os geochronology

The Re-Os data for pyrite samples from the stratabound orebody are reported in Table 3 and graphically shown in Figure 13. Three of the four pyrite samples possess Re concentrations of 26 to 31.9 ppb, with the remaining one containing 1.1 ppb Re. The total Os concentrations range from 31 to 124.7 ppt. With the exception of the relatively low Re sample, the sample set has elevated $^{187}Re/^{188}Os$ (~2400 to 15000) and $^{187}Os/^{188}Os$ (~7.6 to 39) values. The Re-Os data for all samples possess high error correlation (*rho*) values (>0.92). These features characterise samples XQ10, 24 and 25 as low-level highly radiogenic sulphides, which means that the bulk Os, especially ^{187}Os predominately consists of radiogenic ^{187}Os ($^{187}Os^{r}$), rather than common Os that was incorporated into the pyrite during its formation (i.e., common Os) (Stein et al. 2000; Selby et al. 2009). Including the error correlation value, *Isoplot* cannot solve a best fit for the Re-Os data of the pyrite samples. This is, in part, due to associated uncertainty of the $^{187}Re/^{188}Os$ and $^{187}Os/^{188}Os$ values (~2.3 to 12%), and the *rho* values (>0.92), which are calculated from the $^{187}Re/^{188}Os$, $^{187}Os/^{188}Os$, and $^{187}Re/^{187}Os$ values and their uncertainties (Cumming et al. 1972). Not including the *rho* value *Isoplot* calculates a Model 3 (assumes that the scatter about the degree of fit is the result of the assigned uncertainties and an unknown, but normally distributed

variation in the initial $^{187}Os/^{188}Os$ values) date for the Re-Os data of 142 ± 47 Ma, with an initial $^{187}Os/^{188}Os$ value of 1.2 ± 3.5 (MSWD = 7.8).

Discussion

Nature and origin of ore-forming fluids

Fluid inclusions in diopside from the uneconomic skarn exhibit high homogenization temperatures (450-600 ºC) with high, but variable salinities (13-58 wt. % NaCl equiv., Fig. 10), features commonly cited as evidence for magmatic hydrothermal fluids (Meinert et al. 2003). The high and low salinity fluid inclusions in diopside have similar homogenization temperatures (Fig. 10), potentially indicating fluid unmixing during the skarn formation. Similar observations have been made for garnet and diopside in skarn mineral deposits elsewhere (Xiao et al. 2002; Meinert et al. 2005; Bodnar et al. 2014). Field relations indicate that this magmatic hydrothermal fluid was most likely sourced from the Jitou stock and/or the underlying magma chamber. The banded quartz-pyrite veins (Fig. 6I) are paragenetically coeval or slightly postdate retrograde alteration assemblages (Fig. 8). Fluid inclusions hosted by quartz grains from the veins have moderate homogenization temperatures (290-360 º) and moderate to low salinities (5-12 wt. % NaCl equiv.; Fig. 10), comparable to those documented in retrograde alteration assemblages of skarn deposits (Meinert et al. 1997; Xiao et al. 2002; Meinert et al. 2005; Bodnar et al. 2014).

Fluid inclusions hosted by quartz grains from quartz-sulfide veinlets beneath the stratabound massive sulfide ore possess moderate-low homogenization temperatures (200-300 ºC) and salinities (2-10 wt. % NaCl equiv.; Fig. 10), which are slightly lower than those in banded quartz of the skarn ore, but are comparable with the fluids associated with the retrograde alteration assemblages in typical skarn deposits (Bodnar et al. 2014). Moreover, these fluid inclusion

481 characteristics are in sharp contrast to those documented in typical SEDEX deposits (Nesbitt et al.
482 1984; Leach et al. 2004). For example, in Red Dog deposit, fluid inclusions hosted by quartz
483 have significant lower homogenization temperatures and salinities (typically < 230 °C and 5 wt. %
484 NaCl equiv; Leach et al. 2004). The homogenization temperatures obtained in this study
485 represent a minimum estimate for temperatures of the ore-forming fluids, the values, however,
486 are obviously higher than homogenization temperatures of fluid inclusions from typical SEDEX
487 deposits (Leach et al., 2005) and measurements for modern Zn and Pb rich sedimentary brines
488 (60-160 °C), which are believed to be the modern analogues of SEDEX ore-forming fluids
489 (Cooke et al. 2000).

490 Based on the average homogenization temperatures (Fig. 10), the calculated $\delta^{18}O$ values of
491 fluids associated with quartz from the banded skarn ore (328 ± 46 °C) and quartz-pyrite veins
492 (258 ± 42 °C) hosted in sandstone are 6.22 ± 1.59 ‰ and 6.81 ± 2.76 ‰, respectively (Fig. 11).
493 These values confirm a magmatic origin for the ore-forming fluids and that both types of
494 mineralization may have precipitated from the same fluid system. Alteration assemblages in
495 conduit pipes beneath stratabound orebody in classic SEDEX deposits are expected to record a
496 mixing fluid between deep circulated hydrothermal fluid and seawater (Davies et al. 1990; Jiang
497 et al. 1998; Cooke et al. 2000; Slack et al. 2015). Oxygen isotope compositions of carbonates
498 (dolomite, kutnohorite, manganosiderite and calcite) suggests that the fluids responsible for
499 SEDEX Pb-Zn mineralization at the vent site of Sudbury Basin have $\delta^{18}O$ values of ~-1 ‰
500 (Davies et al. 1990). In contrast, the quartz-pyrite vein networks hosted by the Gaolishan
501 Formation sandstone have oxygen isotopes that are significantly heavier than the fluid typical of
502 SEDEX systems, arguing against a SEDEX fluid origin.

503 In summary, fluid inclusions in quartz from banded skarn ore and pyrite-quartz veins hosted
504 in Gaolishan Formation sandstone, the latter having long been considered to be a product of
505 SEDEX mineralization (Gu et al. 2000; Gu et al. 2007; Guo et al. 2011), have broadly
506 comparable homogenization temperatures, calculated salinities, and $\delta^{18}O$ values. The values are
507 also comparable to those documented in retrograde alteration assemblages from typical skarn
508 deposits, both locally in Tongling area (Xiao et al. 2002; Wang and Ni 2009) and globally
509 (Meinert et al. 2005; Bodnar et al. 2014). In contrast, these features are distinctly different from
510 those observed in typical SEDEX deposits and their modern analogues (Davies et al. 1990; Jiang
511 et al. 1998; Cooke et al. 2000; Slack et al. 2015). Taken together, we favour a magmatic origin
512 for the fluid associated with the quartz-pyrite veins at Xinqiao.
513
514 **Timing of mineralization**
515 The SIMS zircon U-Pb data (Fig. 12) suggest that the marginal phase of the Jitou stock (Fig.
516 6B) crystallized at 138.5 ±1.1 Ma, whereas the quartz diorite (Fig. 6C) was emplaced at 130.6
517 ±1.1 Ma. The present SIMS zircon U-Pb age (138.5 ±1.1 Ma) of the Jitou stock is younger than a
518 previous SHRIMP zircon U-Pb age (146.4 ± 4.3 Ma; Wu et al. (2009), but is within analytical
519 uncertainty of an earlier SHRIMP zircon age (140.4 ± 2.2 Ma; Wang et al. (2004). The samples
520 dated by Wu et al. (2009) and Wang et al. (2004) were monzonite and quartz diorite from the
521 Jitou stock, which exhibit intensive propylitic alteration as observed in this study. Although there
522 are textural variations across the Jitou stock, no crosscutting relationships has been observed
523 between the central and marginal phases. As a result, the textural and compositional changes
524 across the pluton is assumed to be controlled by cooling and fractional crystallization. In this
525 case, a multi-stage intrusive history is not favored. Further, a prolonged crystallization history is

526 excluded considering the small volume of the Jitou stock (Fig. 3A-B) and thermal modeling
527 results that suggest a single intrusive event with a size of 160 km^3 can only sustain hydrothermal
528 circulation and near-surface geothermal activity for approximately 800,000 years (Cathles et al.
529 1997). Consequently, the difference between the two SHRIMP zircon U-Pb ages (Wang et al.
530 2004; Wu et al. 2009) and the new SIMS data is most likely caused by bias between labs and
531 methods as demonstrated by Li et al. (2015), although contamination from inheritance cannot be
532 precluded (Mezger and Krogstad 1997; Schoene 2014). Based on the discussion above, our
533 SIMS U-Pb age is considered as the best estimate for the crystallization timing of Jitou stock
534 (Fig. 12A). The alteration-free diorite porphyry dike is ~8 Ma younger than the Jitou stock,
535 indicating a magmatic activity after the emplacement of the Jitou stock.

536 The Re-Os data (not including the *rho* values) of the 4 massive pyrite samples from the
537 stratabound orebody yield a Model 3 Re-Os date of 142 ± 47 Ma (initial $^{187}Os/^{188}Os$ = 1.2 ± 3.5,
538 Fig. 13). The degree of scatter (MWSD = 7.8) about the best fit line of the Re-Os data is beyond
539 that that can be solely explained by analytical uncertainties (Wendt and Carl 1991). The possible
540 reasons to account for the scatter are: (1) open system behavior of Re-Os isotopic system in these
541 pyrite samples (Nakai et al. 1993); (2) multiple pyrite generations in multiple mineralization
542 events (different t, typically different initial $^{187}Os/^{188}Os$ values); (3) prolonged mineralization
543 duration from a single fluid sources (different t, similar $^{187}Os/^{188}Os$ values) (Hnatyshin et al.
544 2015); and (4) simultaneously mineralization from multiple sources fluid (same t, different
545 $^{187}Os/^{188}Os$ values) (Ostendorf et al. 2015).

546 With the exception of sample XQ15, none of Re-Os data for pyrite of this study fall along a
547 ~320 Ma reference line (Fig. 13). Sample XQ15 yields a positive initial $^{187}Os/^{188}Os$ value (0.5) at
548 320 Ma (Table 3). The remaining samples (XQ10, 24 and 25) yield significant negative initial

549 $^{187}Os/^{188}Os$ values (-5.4 to -40.6) at 320 Ma (Table 3), which would suggest that if these samples
550 were formed at ~320 Ma the Re-Os systematics have been significantly disturbed/reset.

551 Further, if we consider samples XQ10, 24, 25 only, the Re-Os data yield a highly imprecise
552 Model 3 data (153 ±160 Ma; Fig. 13) with an initial $^{187}Os/^{188}Os$ value of 0 ± 26 (MWSD = 151).
553 The decrease in precision of the Re-Os data is likely caused by the removal of sample XQ15,
554 which given its low $^{187}Re/^{188}Os$ and $^{187}Os/^{188}Os$ values relative to samples XQ10, 24, 25, may
555 have aided in anchoring the regression line. Additionally, the low precision in the Re-Os data is
556 likely due to highly variable initial $^{187}Os/^{188}Os$ values. Based on above discussion, the variability
557 in the initial$^{187}Os/^{188}Os$ values could be explained by the penecontemporaneous formation of the
558 sulfides from fluids with different $^{187}Os/^{188}Os$ values, and/or inheritance of $^{187}Os/^{188}Os$ values
559 from the country rock through fluid-rock interactions, and/or incomplete resetting of the Re-Os
560 systematics of older pyrite. In addition, Os out of equilibrium in massive pyrite sample due to Os
561 isotopes exchange by solid-state diffusion in pyrite (Brenan et al. 2000) can also account for the
562 scatter observed in this study.

563 Although the Re-Os data yield a poorly-defined best fit line, the Re-Os data of the pyrite
564 samples yield a date that, including uncertainty, overlaps with the age of the Jitou stock (Fig.
565 12A). In addition, this age, within uncertainty, agrees with the 112.6 ± 7.8 Ma pyrite Rb-Sr and
566 the 126 ± 11 Ma pyrite Re-Os mineralization age with samples collected from the stratabound
567 orebody (Wang et al. 2005; Xie et al. 2009), and a recently published quartz fluid inclusion Rb-
568 Sr date representing the age of quartz-pyrite veins hosted by sandstone is 138± 2.3 Ma (Zhang et
569 al. 2015).

570 However, all these early Cretaceous mineralization ages are significantly younger than the
571 319 ± 13 Ma (MSWD = 16) pyrite Re-Os data representing the “age” of pyrite-quartz veinlets

572 hosted by sandstone beneath the stratabound orebody (Guo et al. 2011). The samples of Guo et al.
573 (2011) were collected frompyrite-quartz vein networks hosted by Gaolishan Formation sandstone
574 described in this study (Fig. 6O) and Zhang et al. (2015). But both previous (Wang and Ni 2009)
575 and this study report fluid inclusions data, that is indicative of a magmatic origin. This magmatic
576 origin is most likely related with the Jitou stock, as supported by the 138 ± 2.3 Ma quartz fluid
577 Rb-Sr (Zhang et al. 2015), which is identical to the emplacement age of the Jitou stock (Fig. 12).
578
579 As discussed above, the mineralization of the stratabound orebody and the quartz-pyrite
580 veins hosted by sandstone is, at least in part, associated with a Cretaceous hydrothermal event,
581 likely genetically related to the Jitou stock, as confirmed by the fluid inclusion and oxygen
582 isotope data. However, the age presented here has large uncertainties, and the quartz fluid
583 inclusion Rb-Sr system has uncertainties related to multiple generations of fluid inclusions. This
584 proposes the requirement for additional accurate and precise geochronology to better constrain
585 the mineralization age, and thus the genesis and ore-forming processes of Xinqiao.
586
587 **A Cretaceous carbonate replacement deposit**
588 As discussed above, the nature of ore-forming fluids and mineralisation ages invoke for a
589 Cretaceous magmatic origin for the Xinqiao deposit, presumably genetically related to the
590 Cretaceous Jitou stock and potential associated intrusions at depth. This magmatic model for the
591 Xinqiao deposit is further supported by several lines of evidence. (1) The close spatial
592 association between the Cretaceous intrusions and the stratabound massive sulfide orebody (Fig.
593 3A-C), and the zoned metal distribution grading from magnetite through chalcopyrite to
594 auriferous pyrite and then Zn-Pb sulfides well correlated with distance from the Jitou stock (Fig.

595 5A, B). (2). Coarse grained pyrite (Fig. 6K, 7A) is common in the stratabound orebody at
596 Xinqiao, which contrasts to the fine grained nature of pyrite typically occurring in SEDEX
597 deposits (Leach et al. 2005). The locally presented massive, colloform and laminated ore textures
598 (Fig. 6J-L, 7B-C) at Xinqiao are not diagnostic of SEDEX deposits as they are also widely
599 present in skarn deposits (Meinert 1982; Sato 1984). (3) The quartz-pyrite vein networks hosted
600 by Gaolishan Formation sandstone are locally broadly perpendicular to the stratabound orebody,
601 but are controlled by brittle fractures (803-Geological-Team 1971; Pan and Dong 1999; Gu et al.
602 2000; Guo et al. 2011). This contrasts to synsedimentary faults that are characteristic of many
603 SEDEX deposits (Large 1983; Goodfellow et al. 1993). (4) The pyrite-quartz networks in the
604 Gaolishan Formation sandstone lack zoned alteration halos (Wang and Ni 2009; Guo et al. 2011;
605 Zhang et al. 2015) and are predominately comprised of coarse grained Au-enriched pyrite (Fig.
606 6O, 7A). This is different from typical feeder zones of SEDEX deposit, e.g., Sullivan Pb-Zn
607 deposit in British Columbia and Pomorzany Pb-Zn deposit in Poland, where the fluid conduits
608 have zoned geometries with the sulphides exhibiting fine-grained colloform textures, with
609 abundant quartz, tourmaline and Fe-Mn carbonates alteration assemblages, and the sulfides are
610 rarely rich in Au (Jiang et al. 1998; Leach et al. 2005).
611 In summary, ore-forming fluids at Xinqiao have similar temperatures, salinities and $\delta^{18}O$
612 values with those observed in typical skarn deposits, but are distinctly different from those
613 documented in SEDEX deposits and their modern analogues. The close association of the
614 mineralization with magmatism, metal zoning, ore distribution patterns and fluid nature all show
615 a magmatic affinity. The field occurrences coupled with geochemical and geochronological data
616 suggest that the Xinqiao deposit can be best classified as a carbonate replacement deposit
617 associated with early Cretaceous magmatism.

618

619 **General patterns of stratabound massive ore deposits and implications for exploration**

620 Extensive sulfur isotope studies have been conducted in an attempt to constrain the genesis
621 of stratabound massive sulfide deposits along MLYMB. As presented in Figure 14 stratabound
622 massive sulfide deposits have pyrite $\delta^{34}S$ values ranging from -1.1 to 7.7 ‰ with an average of
623 3.8 ‰ (n = 128), with exception of three analyses (-9, -13, 11 ‰, Zhou et al. 1983; Zhou 1984;
624 Zhao et al. 1985; Liu and Liu 1991; Pan and Dong 1999; Xu et al. 2004; Li 2006; Xu et al. 2010).
625 The sulfur isotope data are comparable with those of Cretaceous intrusions and associated skarn
626 and porphyry deposits, which show limited variations between -1.3 and 7.0 ‰, with a mean of
627 2.8 ‰ (n = 56, Pan and Dong 1999; Xu et al. 2010). In contrast, the diagenetic pyrite samples
628 from the major host rocks of the stratabound massive sulfide deposits, Carboniferous carbonates,
629 have negative $\delta^{34}S$ values with significant fluctuations between -35.4 and -17.6 ‰ (n = 10, Zhou
630 1984; Xu et al. 2010). Thus, pyrite sulfur isotope data suggest that the stratabound massive
631 sulfide deposits are most likely related to the spatially associated Cretaceous magmatic systems,
632 and have limited contribution from sedimentary sulfur.

633 Mineralization age is the most critical information to understand the genesis of stratabound
634 massive sulfide deposits in MLYMB. As summarized in Table 3 and Figure 15, both
635 Carboniferous and Cretaceous ages are reported. Although the magmatic rocks and associated
636 porphyry-skarn deposits were broadly formed between 148 and 130 Ma, the reported
637 mineralization ages of stratabound massive sulfide deposits derived from pyrite Rb-Sr and pyrite
638 Re-Os predominately are based on Xinqiao and show significant scatter (Fig. 15; (Meng et al.
639 2004; Wang et al. 2005; Xie et al. 2009; Guo et al. 2011; Zhang et al. 2015). As discussed earlier,
640 there is a need for further accurate and precise ages.

641 Geochemical anomaly mapping is one the most important guidance for mineral exploration.
642 Soil Cu, Pb, Zn, Au and Ag geochemical anomaly map in the Tongling area (Fig. 16, Jiujiang
643 conference communication, 2010) shows a strong concentric zonation around Miocene intrusions,
644 which are the same as documented in Mankayan intrusion-centered Cu-Au district, Philippines
645 (Chang et al. 2011). This is different to the geochemical anomalies around SEDEX deposits,
646 which are stratigraphically controlled, as demonstrated by Lambert and Scott (1973) in the HYC
647 deposit, Australia, where Mn and to lesser extent Pb and Zn, occur in dolomites in a narrow
648 envelope surrounding the stratabound orebody, and extends along the favourable horizon at the
649 base of pyrite shale member for at least 23 km.
650 Given the close spatial association between the stratabound massive sulfide deposits and
651 Cretaceous magmatism, magmatic affinity of the alteration assemblages and geochemical data,
652 as well as the structural/unconformity controlled position of the ore body, we propose that a
653 promising exploration target for stratabound massive sulfide deposits is the convergence zone
654 where the Cretaceous intrusions intrude or overprint the unconformity between the Late
655 Devonian Wutong and the Early Carboniferous Gaolishan Formations. Early Cretaceous
656 intrusions with known associated stratabound massive sulfide deposits may also contain Cu (Mo
657 and Au) resources at depth as porphyry/skarn mineralization, as supported by the newly
658 discovered porphyry Cu-Mo deposit at depth of Dongguashan stratabound massive sulfide
659 deposit (Yuan et al. 2014).
660
661 **Conclusions**
662 Fluid inclusions hosted by prograde diopside yield homogenization temperatures between
663 450-600 ^{o}C and calculated salinities of 13-58 wt. % NaCl equiv. While fluid inclusions hosted by

664 quartz from the banded skarn ore and pyrite-quartz vein networks in the Gaolishan Formation
665 sandstone have homogenization temperatures of 290-360 and 200-300 °C, with calculated
666 salinities of 5-12 and 2-10 wt. % NaCl equiv respectively. Quartz grains from the banded skarn
667 ore and the pyrite-quartz vein networks hosted by Gaolishan Formation sandstone have SIMS
668 $\delta^{18}O$ values of 12.32 ± 0.55 (2 SD, n = 22) and 15.57 ± 1.92 ‰ (2 SD, n = 60), with calculated
669 fluid $\delta^{18}O$ values of 6.22 ± 1.59 and 6.81 ± 2.76 ‰ based on the average fluid inclusion
670 homogenization temperatures of 328 ± 46 and 258 ± 42 °C of this study, respectively. The SIMS
671 zircon U-Pb data indicate the Jitou stocks was emplaced at 138.5 ±1.1 Ma (2σ, MSWD = 0.6),
672 and the alteration-free diorite porphyry dike was crystalized at 130.6 ±1.1 Ma (2σ, MSWD = 0.1).
673 Massive pyrite ore samples from the stratabound orebody yield a 142 ± 47 Ma Model 3 age. All
674 the fluid inclusion, oxygen isotope and geochronology data support a magmatic origin, together
675 with the magmatic affinity of the orebody and alteration assemblages with Jitou stock, we
676 classify the Xinqiao deposit as a Carbonate replacement deposit genetic related with the Jitou
677 stock.

678 The spatial association of stratabound massive sulfide orebodies along MLYMB with
679 Cretaceous magmatism, pyrite sulfur isotope and zoned geochemical anomalies all can be
680 explained neatly by a magmatic genetic scenario, although further accurate and precise
681 mineralization dating is needed for further understanding the ore-forming process. The
682 association between stratabound ores with Early Cretaceous magmatism has broad implications
683 for future mineral exploration, with emphasis on conjunction between Cretaceous magmatic
684 intrusions and Early Carboniferous carbonates, particularly around Cretaceous intrusions with
685 associated skarn and porphyry mineralization. Additionally, our model may imply that porphyry

and skarn Cu-Au systems could occur beneath the known stratabound massive sulfide ore deposits in this region.

Acknowledgements

Hao Hu and Sha-Sha Liu assisted with the fieldwork. Hong-Xia Ma, Jiao Li and Xiao-Yan Jiang, Yu Liu, Guo-Qiang Tang are acknowledged for generous help during SIMS U-Pb and SIMS O isotope analysis. This research is jointly supported by the National Natural Science Foundation of China (41325007, 91414301), the National Basic Research Program of China (2012CB416802), and the Nanjing Centre of China Geological Survey. DS acknowledges the support of the TOTAL endowment fund. Comments from Zhao-Shan Chang, Peter Megaw and an anonymous reviewer on an earlier version of this work are acknowledged. Two anonymous reviewers for OGR are also thanked for further improvements of this paper.

References

803-Geological-Team (1971) Reserves report of Xinqiao Cu bearing pyrite deposits, Tonglong, Anhui. Metallurgical Geology Bureau of Anhui Province, pp 141. (In Chinese).

Baumgartner M, Bakker RJ, Doppler G (2014) Re-equilibration of natural H_2O-CO_2-salt-rich fluid inclusions in quartz-Part 1: experiments in pure water at constant pressures and differential pressures at 600 ºC. Contributions to Mineralogy and Petrology 168:1-14. doi: doi:10.1007/S00410-014-1017-3.

Bodnar RJ, Vityk MO (1994) Interpretation of microthermometric data for H_2O-NaCl fluid inclusions In: Vivo BD, Frezzotti ML (eds) Fluid inclusions in minerals: Methods and applications. Virginia Tech, Blacksburg, VA, pp 117-130.

Bodnar RJ, Lecumberri-Sanchez P, Moncada D, Steele-MacInnis M (2014) 13.5 - Fluid Inclusions in Hydrothermal Ore Deposits In: Turekian HDHK (ed) Treatise on Geochemistry (Second Edition). Elsevier, Oxford, pp 119-142.

Brenan JM, Cherniak DJ, Rose LA (2000) Diffusion of osmium in pyrrhotite and pyrite: implications for closure of the Re-Os isotopic system. Earth and Planetary Science Letters 180:399-413. doi: doi:10.1016/S0012-821x(00)00165-5.

Cathles LM, Erendi AHJ, Barrie T (1997) How long can a hydrothermal system be sustained by a single intrusive event? Economic Geology 92:766-771. doi: 10.2113/gsecongeo.92.7-8.766.

Chang ZS, Hedenquist JW, White NC, Cooke DR, Roach M, Deyell CL, Garcia J, Gemmell JB, McKnight S, Cuison AL (2011) Exploration Tools for Linked Porphyry and Epithermal Deposits: Example from the Mankayan Intrusion-Centered Cu-Au District, Luzon, Philippines. Economic Geology 106:1365-1398. doi: 10.2113/econgeo.106.8.1365.

Cooke DR, Bull SW, Large RR, McGoldrick PJ (2000) The importance of oxidized brines for the formation of Australian proterozoic stratiform sediment-hosted Pb-Zn (sedex) deposits. Economic Geology and the Bulletin of the Society of Economic Geologists 95:1-17.

Creaser RA, Papanastassiou DA, Wasserburg GJ (1991) Negative Thermal Ion Mass-Spectrometry of Osmium, Rhenium, and Iridium. Geochimica Et Cosmochimica Acta 55:397-401. doi: 10.1016/0016-7037(91)90427-7.

Cumming G, Rollett J, Rossotti F, Whewell R (1972) Statistical methods for the computation of stability constants. Part I. Straight-line fitting of points with correlated errors. Journal of the Chemical Society, Dalton Transactions:2652-2658.

Davies JF, Leroux MV, Whitehead RE, Goodfellow WD (1990) Oxygen-Isotope Composition and Temperature of Fluids Involved in Deposition of Proterozoic Sedex Deposits, Sudbury Basin, Ontario. Canadian Journal of Earth Sciences 27:1299-1303. doi: 10.1139/e90-139.

Ding X, Jiang S-Y, Ni P, Gu L-X, Jiang Y-H (2005) Zircon SIMS U–Pb geochronology of host granitoids in Wushan and Yongping copper deposits, Jiangxi Province. Geological Journal of China Universities 11:383-389.

Goldstein RH, Reynolds TJ (1994) Systematics of fluid inclusions in diagenetic minerals. Society for Sedimentary Geology, US.

Goodfellow W, Lydon J, Turner R (1993) Geology and genesis of stratiform sediment-hosted (SEDEX) zinc-lead-silver sulphide deposits. Geological Association of Canada Special Paper 40:201-251.

Gu LX, Hu WX, He JX, Ni P, Xu KQ (2000) Regional variations in ore composition and fluid features of massive sulphide deposits in South China: Implications for genetic modelling. Episodes 23:110-118.

Gu LX, Zaw K, Hu WX, Zhang KJ, Ni P, He JX, Xu YT, Lu JJ, Lin CM (2007) Distinctive features of Late Palaeozoic massive sulphide deposits in South China. Ore Geology Reviews 31:107-138. doi: 10.1016/j.oregeorev.2005.01.002.

Guo JL, Gao S, Wu YB, Li M, Chen K, Hu ZC, Liang ZW, Liu YS, Zhou L, Zong KQ, Zhang W, Chen HH (2014) 3.45 Ga granitic gneisses from the Yangtze Craton, South China: Implications for Early Archean crustal growth. Precambrian Research 242:82-95. doi: 10.1016/j.precamres.2013.12.018.

Guo WM, Lu JJ, Jiang SY, Zhang RQ, Qi L (2011) Re-Os isotope dating of pyrite from the footwall mineralization zone of the Xinqiao deposit, Tongling, Anhui Province: Geochronological evidence for submarine exhalative sedimentation. Chinese Science Bulletin 56:3860-3865. doi: 10.1007/s11434-011-4770-y.

Hnatyshin D, Creaser RA, Wilkinson JJ, Gleeson SA (2015) Re-Os dating of pyrite confirms an early diagenetic onset and extended duration of mineralization in the Irish Zn-Pb ore field. Geology 43:143-146. doi: 10.1130/G36296.1.

Jiang SY, Palmer MR, Slack JF, Shaw DR (1998) Paragenesis and chemistry of multistage tourmaline formation in the Sullivan Pb-Zn-Ag deposit, British Columbia. Economic Geology and the Bulletin of the Society of Economic Geologists 93:47-67. doi: 10.2113/gsecongeo.93.1.47.

Lambert I, Scott K (1973) Implications of geochemical investigations of sedimentary rocks within and around the McArthur zinc-lead-silver deposit, Northern Territory. Journal of Geochemical Exploration 2:307-330.

Large D (1983) Sediment-hosted massive sulphide lead-zinc deposits: an empirical model In: Sangster DF (ed) Short Course Handbook. Mineral. Assoc. Canada, Canada, pp 1-30.

Leach D, Sangster D, Kelley K, Large R, Garven G, Allen C, Gutzmer J, Walters S (2005) Sediment-hosted lead-zinc deposits: A global perspective. Economic Geology 100:561-607.

768 Leach DL, Marsh E, Emsbo P, Rombach CS, Kelley KD, Anthonty M (2004) Nature of
769 hydrothermal fluids at the shale-hosted Red Dog Zn-Pb-Ag deposits, Brooks Range, Alaska.
770 Economic Geology 99:1449-1480. doi: 10.2113/99.7.1449.

771 Li DW, Fu ZR (1991) Multiple thrusting systems in the Middle and Lower Yangtze Metallognic
772 Belt and their sinificance in mineralization. Earth Science-Journal of China University of
773 Geosciences:670, 680. (In Chinese).

774 Li J-W, Li X-H, Pei R-F, Mei Y-X, Wang Y-L, Qu W-J, Huang X-B, Zang W-S (2007) Re-Os
775 Age of Molybdenite from the Southern Ore Zone of the Wushan Copper Deposit, Jiangxi
776 Province, and Its Geological Significance. Acta Geologica Sinica 81:801-807.

777 Li X-H, Liu Y, Li Q-L, Guo C-H, Chamberlain KR (2009) Precise determination of Phanerozoic
778 zircon Pb/Pb age by multicollector SIMS without external standardization. Geochemistry,
779 Geophysics, Geosystems 10:1-21. doi: 10.1029/2009gc002400.

780 Li XH, Li WX, Li ZX, Liu Y (2008) 850-790 Ma bimodal volcanic and intrusive rocks in
781 northern Zhejiang, South China: A major episode of continental rift magmatism during the
782 breakup of Rodinia. Lithos 102:341-357. doi: 10.1016/j.lithos.2007.04.007.

783 Li XH, Li WX, Li QL, Wang XC, Liu Y, Yang YH (2010a) Petrogenesis and tectonic
784 significance of the similar to 850 Ma Gangbian alkaline complex in South China: Evidence
785 from in situ zircon U-Pb dating, Hf-O isotopes and whole-rock geochemistry. Lithos 114:1-
786 15. doi: 10.1016/j.lithos.2009.07.011.

787 Li XH, Li WX, Wang XC, Li QL, Liu Y, Tang GQ, Gao YY, Wu FY (2010b) SIMS U-Pb zircon
788 geochronology of porphyry Cu-Au-(Mo) deposits in the Yangtze River Metallogenic Belt,
789 eastern China: Magmatic response to early Cretaceous lithospheric extension. Lithos
790 119:427-438. doi: 10.1016/j.lithos.2010.07.018.

791 Li XH, Tang GQ, Gong B, Yang YH, Hou KJ, Hu ZC, Li QL, Liu Y, Li WX (2013) Qinghu
792 zircon: A working reference for microbeam analysis of U-Pb age and Hf and O isotopes.
793 Chinese Science Bulletin 58:4647-4654. doi: 10.1007/s11434-013-5932-x.

794 Li XH, Liu XM, Liu YS, Su L, Sun WD, Huang HQ, Yi K (2015) Accuracy of LA-ICPMS
795 zircon U-Pb age determination: An inter-laboratory comparison. Sci China Earth Sci
796 58:1722-1730. doi: 10.1007/s11430-015-5110-x.

797 Li XJ (2006) Study of Ore Formation Conditions and Ore Deposit Models in Tongling Area,
798 Anhui Province, China. China University of Geosciences, Beijing, pp 129. (In Chinese with
799 English Abstract).

800 Li ZX, Li XH (2007) Formation of the 1300-km-wide intracontinental orogen and postorogenic
801 magmatic province in Mesozoic South China: A flat-slab subduction model. Geology
802 35:179-182. doi: 10.1130/G23193a.1.

803 Liu YQ, Liu ZL, Yang CX (1984) Stable isotope studies of the Dongguashan Copper deposit in
804 Tongling Prefecture, Anhui Province. Bulletin of the Institute of Mineral Deposits, Chinese
805 Academy of Geological Sciences:70-101.

806 Liu YQ, Liu ZL (1991) Isotopes geochemistry and genesis of the stratiform massive copper
807 (iron-sulfur) deposits in Tongling area, Anhui province. Bulletin of the Institute of Mineral
808 Deposits, Chinese Academy of Geological Sciences 24:47-114. (In Chinese).

809 Lu S-M (2007) The Magmatism and Fluid Mineralizationin Shizishan Copper-gold Ore-field of
810 Tongling, Anhui Province. Hefei University of Technology, pp 1-179.

811 Ludwig KR (2003) User's manual for Isoplot 3.00: a geochronological toolkit for Microsoft
812 Excel. Kenneth R. Ludwig.

813 Mao J-W, Wang Y-T, Lehmann B, Yu J-J, Du A-D, Mei Y-X, Li Y-F, Zang W-S, Stein HJ,
814 Zhou T-F (2006) Molybdenite Re–Os and albite ^{40}Ar ^{39}Ar dating of Cu–Au–Mo and
815 magnetite porphyry systems in the Yangtze River valley and metallogenic implications. Ore
816 Geology Reviews 29:307-324.

817 Mao JW, Xie GQ, Duan C, Pirajno F, Ishiyama D, Chen YC (2011) A tectono-genetic model for
818 porphyry-skarn-stratabound Cu-Au-Mo-Fe and magnetite-apatite deposits along the Middle-
819 Lower Yangtze River Valley, Eastern China. Ore Geology Reviews 43:294-314. doi:
820 10.1016/j.oregeorev.2011.07.010.

821 Matsuhisa Y (1974) $^{18}O/^{16}O$ ratios for NBS-28 and some silicate reference samples.
822 Geochemical Journal 8:103-107.

823 Meinert LD (1982) Skarn, Manto, and Breccia Pipe Formation in Sedimentary-Rocks of the
824 Cananea Mining District, Sonora, Mexico. Economic Geology 77:919-949.

825 Meinert LD, Hefton KK, Mayes D, Tasiran I (1997) Geology, zonation, and fluid evolution of
826 the big Gossan Cu-Au skarn deposit, Ertsberg district: Irian Jaya. Economic Geology and the
827 Bulletin of the Society of Economic Geologists 92:509-534. doi:
828 10.2113/gsecongeo.92.5.509.

829 Meinert LD, Hedenquist JW, Satoh H, Matsuhisa Y (2003) Formation of anhydrous and hydrous
830 skarn in Cu-Au ore deposits by magmatic fluids. Economic Geology and the Bulletin of the
831 Society of Economic Geologists 98:147-156. doi: Doi 10.2113/98.1.147.

832 Meinert LD, Dipple G, Nicolescu S (2005) World skarn deposits. Economic Geology 100:299-
833 336.

834 Meng YF, Yang ZS, Zeng PS, Xu WY, Wang XC (2004) Tentative temporal constraints of ore-
835 forming fluid systems in Tongling metallogenic province. Mineral Deposits 23:271-280. (In
836 Chinese with English Abstract).

837 Mezger K, Krogstad EJ (1997) Interpretation of discordant U-Pb zircon ages: An evaluation.
838 Journal of Metamorphic Geology 15:127-140. doi: DOI 10.1111/j.1525-1314.1997.00008.x.

839 Nakai S, Halliday AN, Kesler SE, Jones HD, Kyle JR, Lane TE (1993) Rb-Sr Dating of
840 Sphalerites from Mississippi Valley-Type (Mvt) Ore-Deposits. Geochimica Et
841 Cosmochimica Acta 57:417-427. doi: Doi 10.1016/0016-7037(93)90440-8.

842 Nesbitt BE, Longstaffe FJ, Shaw DR, Muehlenbachs K (1984) Oxygen Isotope Geochemistry of
843 the Sullivan Massive Sulfide Deposit, Kimberley, British-Columbia. Economic Geology
844 79:933-946. doi: 10.2113/gsecongeo.79.5.933.

845 Ostendorf J, Henjes-Kunst F, Mondillo N, Boni M, Schneider J, Gutzmer J (2015) Formation of
846 Mississippi Valley-type deposits linked to hydrocarbon generation in extensional tectonic
847 settings: Evidence from the Jabali Zn-Pb-(Ag) deposit (Yemen). Geology 43:1055-1058. doi:
848 10.1130/G37112.1.

849 Pan YM, Dong P (1999) The Lower Changjiang (Yangzi/Yangtze River) metallogenic belt, east
850 central China: intrusion- and wall rock-hosted Cu-Fe-Au, Mo, Zn, Pb, Ag deposits. Ore
851 Geology Reviews 15:177-242. doi: Doi 10.1016/S0169-1368(99)00022-0.

852 Roedder E (1984) Fluid Inclusions. Mineralogical Society of America, US.

853 Sato T (1984) Manto type copper deposits in Chile: a review. Bulletin of the geological survey of
854 Japan 35:565-582.

855 Schoene B (2014) 4.10 - U–Th–Pb Geochronology In: Turekian HDHK (ed) Treatise on
856 Geochemistry (Second Edition). Elsevier, Oxford, pp 341-378.

857 Selby D, Creaser RA (2001) Re-Os geochronology and systematics in molybdenite from the
858 Endako porphyry molybdenum deposit, British Columbia, Canada. Economic Geology and
859 the Bulletin of the Society of Economic Geologists 96:197-204. doi: Doi 10.2113/96.1.197.

860 Selby D, Kelley KD, Hitzman MW, Zieg J (2009) Re-Os sulfide (bornite, chalcopyrite, and
861 pyrite) systematics of the carbonate-hosted copper deposits at Ruby Creek, Southern Brooks
862 Range, Alaska. Economic Geology 104:437-444.

863 Slack JF, Selby D, Dumoulin JA (2015) Hydrothermal, Biogenic, and Seawater Components in
864 Metalliferous Black Shales of the Brooks Range, Alaska: Synsedimentary Metal Enrichment
865 in a Carbonate Ramp Setting. Economic Geology 110:653-675.

866 Sláma J, Košler J, Condon DJ, Crowley JL, Gerdes A, Hanchar JM, Horstwood MS, Morris GA,
867 Nasdala L, Norberg N (2008) Plešovice zircon—a new natural reference material for U–Pb
868 and Hf isotopic microanalysis. Chemical Geology 249:1-35.

869 Stacey Jt, Kramers J (1975) Approximation of terrestrial lead isotope evolution by a two-stage
870 model. Earth and Planetary Science Letters 26:207-221.

871 Stein HJ, Morgan JW, Schersten A (2000) Re-Os Dating of Low-Level Highly Radiogenic
872 (LLHR) Sulfides:The Harnas Gold Deposit, Southwest Sweden, Records Continental-Scale
873 TectonicEvents. Economic Geology 95:1657-1671. doi: 10.2113/gsecongeo.95.8.1657.

874 Wan TF (2012) The Tectonics of China: Data, Maps and Evolution. Springer, Beijing, China.

875 Wang GG, Ni P (2009) Fluid inclusions study for the pyrite vein beneath Xinqiao stritiform
876 massive Cu deposit. Acta Mineralogica Sinica. pp 256 (In Chinese).

877 Wang YB, Liu DY, Meng YF, Zeng PS, Yang ZS, Tian SH (2004) SHRIMP U-Pb
878 geochronology of the Xinqiao Cu-S-Fe-Au deposit in the Tongling ore district, Anhui.
879 Geology in China 31:169-173.

880 Wang YB, Tang SH, Wang JH, Zeng PS, Yang ZS, Meng YF, Tian SH (2005) Rb-Sr Dating the
881 Pyrite of the Xinqiao Cu-S-Fe-Au Deposit, Tongling, Anhui Province. Geological Review
882 50:538-542. (In Chinese with English Abstract).

883 Wendt I, Carl C (1991) The Statistical Distribution of the Mean Squared Weighted Deviation.
884 Chemical Geology 86:275-285. doi: Doi 10.1016/0168-9622(91)90010-T.

885 Wu C-L (1996) ^{40}Ar- ^{39}Ar Chronology of Intrusive Rocks from Tongling. Acta Petrologica Et
886 Mineralogica 15:299-306.

887 Wu GG, Zhang D, Zang WS (2003) Study of tectonic layering motion and layering
888 mineralization in the Tongling metallogenic cluster. Science in China Series D-Earth
889 Sciences 46:852-863. doi: 10.1360/03yd0204.

890 Wu GG, Zhang D, Di YJ, Zang WS, Zhang XX, Song B, Zhang ZY (2009) SHRIMP Zircon U-
891 Pb daing for Intrusions in Tongling mining districts and implications for geodynamics.
892 Science China Earth Sciences 38:630-645. (In Chinese with English Abstract). doi:
893 http://earth.scichina.com:8080/sciD/CN/

894 Wu L-S, Zou X-Q (1997) Re-Os isotopic age study of the Chengmenshan copper deposit, Jiangxi
895 Province. Mineral Deposits 16:376-381.

896 Xiao X, Zhou TF, Fan Y, Xie J, ZHang LJ (2016) LA-ICP-MS in situ trace elements and FE-
897 SEM analysis of pyrite from the Xinqiao Cu-Au-S deposit in Tongling, Anhui and its
898 constraints on the ore genesis. Acta Petrologica Sinica 32:369-376.

899 Xiao XJ, Gu LX, Ni P (2002) Multi-episode fluid boiling in the Shizishan copper-gold deposit at
900 Tongling, Anhui Province: its bearing on ore formation. Science in China Series D-Earth
901 Sciences 45:34-44. doi: Doi 10.1007/Bf02879694.

902 Xie JC, Yang XY, Sun WD, Du JG, Xu W, Wu LB, Wang KY, Du XW (2009)
903 Geochronological and geochemical constraints on formation of the Tongling metal deposits,
904 middle Yangtze metallogenic belt, east-central China. International Geology Review 51:388-
905 421. doi: doi:10.1080/00206810802712004.

906 Xie QQ, Chen TH, Fan ZL, Xu XC, Zhou YF, Shi WB, Xue JJ (2014) Morphological
907 characteristics and genesis of colloform pyrite in Xinqiao Fe-S deposit, Tongling, Anhui
908 Province (in Chinese). Science in China Series D: Earth Sciences 44:2665-2674. (In Chinese
909 with English Abstract).

910 Xu G, Zhou J (2001) The Xinqiao Cu-S-Fe-Au deposit in the Tongling mineral district, China:
911 synorogenic remobilization of a stratiform sulfide deposit. Ore Geology Reviews 18:77-94.
912 doi: Doi 10.1016/S0169-1368(01)00017-8.

913 Xu WY, Yang ZS, Meng YF, Zeng PS, Shi DN, Tian SH, Li HY (2004) Genetic model and
914 dynamic migration of ore-forming fluids in carboniferous exhalation-sedimentary massive
915 sulfide deposits of Tongling district, Anhui Province. Mineral Deposits 23:353-363. (In
916 Chinese with English Abstract).

917 Xu XC, Yin T, Lou JW, Lu SM, Xie QQ, Chu PL (2010) Origin of Dongguashan stratabound
918 Cu-Au skarn deposit in Tongling: Restraints of sulfur isotope. Acta Petrologica Sinica
919 26:2739-2750. (In Chinese with English Abstract).

920 Yang SY, Jiang SY, Li L, Sun Y, Sun MZ, Bian LZ, Xiong YG, Cao ZQ (2011a) Late Mesozoic
921 magmatism of the Jiurui mineralization district in the Middle-Lower Yangtze River
922 Metallogenic Belt, Eastern China: Precise U-Pb ages and geodynamic implications.
923 Gondwana Research 20:831-843. doi: 10.1016/j.gr.2011.03.012.

924 Yang XN, Xu ZW, Lu XC, Jiang SY, Ling HF, Liu LG, Chen DY (2011b) Porphyry and skarn
925 Au-Cu deposits in the Shizishan orefield, Tongling, East China: U-Pb dating and in-situ Hf
926 isotope analysis of zircons and petrogenesis of associated granitoids. Ore Geology Reviews
927 43:182-193. doi: 10.1016/j.oregeorev.2010.09.003.

928 Yuan F, Song YL, Wang SW, Zhou TF, Sun WA (2014) Characteristics of porphyry
929 mineralization in the depth of Dongguashan deposit and its relationship with skarn-type
930 mineralization. Chinese Journal of Geology 49:588-607. (In Chinese with English Abstract).

931 Zhang Y, Shao YJ, Quan W, Liu ZF, Liu QQ (2015) Rb-Sr Isotope Dating of the Fluid
932 Inclusions in Quartz from Quartz-Pyrite Veins in the Footwall of Xinqiao Cu-S-Fe Deposit,
933 Tongling. Geological Review 61:1168-1176.

934 Zhao JH, Zhou MF, Yan DP, Zheng JP, Li JW (2011) Reappraisal of the ages of Neoproterozoic
935 strata in South China: No connection with the Grenvillian orogeny. Geology 39:299-302. doi:
936 10.1130/G31701.1.

937 Zhao R, Xie YH, Yao YY, He WG (1985) S isotopes study for Chengmenshan and Wushan Cu
938 deposits. Chinese Journal of Geology 3:251-258. (In Chinese).

939 Zhou TF, Yu F, Yuan F (2008) Advances on petrogensis and metallogeny study of the
940 mineralization belt of the Middle and Lower Reaches of the Yangtze River area. Acta
941 Petrologica Sinica 24:1665-1678.

942 Zhou TF, ZHang LJ, Yuan F, Fan Y (2010) LA-ICP-MS in situ trace element analysis of pyrite
943 from the Xinqiao C-Au-S Deposit in Tongling, Anhui, and its constraints on the ore genesis.
944 Earth Science Frontiers 17:306-319.

945 Zhou WK, Chen SY, Zhao SL, Cheng QF, Mao JR, Qiu YQ (1983) The Volcanics in north ore
946 zone of the copper deposit in Wushan, Jiangxi Province. Bulletin of Nanjing Institute of
947 Geology and Mineral Resources 4:47-62. (In Chinese).

948 Zhou Z (1984) Genesis for Mashan Au deposit, Tongling. Geological Review 30:467-476. (In
949 Chinese).

950

951 **List of Tables and Figures**

952 **Table 1**. SIMS zircon U-Pb data of the Xinqiao stock quartz diorite and an unaltered diorite
953 porphyry.

954 **Table 2**. SIMS quartz oxygen isotope data of banded quartz veins from the skarn ore and pyrite-
955 quartz veins hosted by the Gaolishan Formation sandstone.

956 **Table3**. Re-Os data of pyrite samples from the stratabound massive orebody at Xinqiao.

957 **Table4**. Published geochronology data for the strataform massive sulfide deposits and
958 Cretaceous intrusions and associated porphyry-skarn deposits along Middle and Lower
959 Metallogenic Belt.

960 **Fig.1**. Geological map showing the igneous rocks distribution in the mining districts along the
961 Middle and Lower Metallogenic Belt, with the insert illustrating the geological setting of China.
962 Revised after Mao et al. (2011).

963 **Fig.2**. Stratigraphic column of sedimentary rocks exposed in the Xinqiao mining area. Revised
964 after 803-Geological-Team (1971).

965 **Fig.3**.A). Geological map of Xinqiao deposit; B-C). Representative cross sections of Xinqiao
966 deposit, with samples location marked in B. Revised after 803-Geological-Team (1971). See text
967 for detailed information.

968 **Fig.4**.Massive pyrite ore occurs as veins in Permian Qixia Formation limestone. Revised after
969 803-Geological-Team (1971).

970 **Fig. 5**. A). Cu, S, Au and Ag grade distribution in the main stratabound orebody at Xinqiao,
971 which shows strong relationship to the distance from the Jitou stock. The location of the Jitou
972 stock is between the exploration lines 15 and 26; B). Distribution of massive pyrite ore, massive
973 chalcopyrite ore, massive pyrite ore, massive magnetite ore and Pb-Zn mineralization at Xinqiao,
974 which show a close association with the Jitou stock exhibiting concentric zoning, see text for
975 discussion. Revised after 803-Geological-Team (1971).

976 **Fig. 6**. Igneous rocks, alteration and mineralization assemblages of the Xinqiao deposit. A).
977 Fresh quartz diorite from the central phase of the Jitou stock; B). Diorite porphyry from the

marginal phase of the Jitou stock, with quartz vein and feldspar dissolution vugs indicating intensive alteration; C). Alteration-free diorite porphyry observed in the open pit; D). Red-brown garnet skarn with hematite and calcite; E). Banded wollastonite skarn in silicified limestone with garnet and diopside, the wollastonite clusters exhibit radiating textures; F).Radiating clusters of epidote in the alterated diorite porphyry; G). Clusters of chlorite in diorite porphyry; H). Pyrite-calcite vein in massive magnetite ore; I). Banded quartz and pyrite veins from the skarn ore; J). Massive pyrite ore comprising massive anhedral grains with a pale colour; K). A cluster of cubic pyrite ore; L). Massive colloform pyrite ore with cluster and vein comprised of crystallized pyrite; M). Massive chalcopyrite ore; N). Sphalerite-pyrite-calcite vein in limestone; O). Pyrite-quartz vein in Gaolishan Formation sandstone, the pyrite are coarse grained. See text for detailed description.

Fig. 7. Photomicrographs and scanning electron microscope (SEM) images illustrating the petrographic characteristics of the sulfides and quartz at Xinqiao. A) Euhedral pyrites grains; B) Anhedral pyrite grains; C) Colloform pyrite grains; D) Massive chalcopyrite ore with pyrite and magnetite; E) Pyrite, quartz and carbonate minerals from garnet bearing skarn ore; F) Anhedral quartz with pyrite grains from pyrite-quartz veins hosted by the Gaolishan Formation sandstone. Pyrite sample from A and B are used for Re-Os dating, quartz grains from E and F are used for SIMS oxygen analysis. See text for details.

Fig.8. Alteration and mineralization paragenesis at Xinqiao. Revised after (803-Geological-Team 1971).

Fig.9. Fluid inclusions hosted by diopside and quartz grains. A-B) Diopside hosted pseudosecondary liquid-vapor fluid inclusions with and without halite minerals from the skarn ore; C) Liquid-vapour two-phase fluid inclusions hosted by quartz grains form the banded pyrite-quartz skarn ore; D) Liquid-vapor two-phase fluid inclusions hosted by quartz grains from the pyrite-quartz veins in the Gaolishan Formation sandstone.

Fig.10. Homogenization temperature-salinity plot of the fluid inclusions associated with the skarn ore and the pyrite-quartz veins in the Gaolishan Formation sandstone. Also presented are the quartz hosted fluid inclusions data from the Red Dog Pb-Zn deposit (Leach et al. 2004). See text for detailed information.

Fig.11. SIMS quartz oxygen isotope data of the quartz bearing skarn ore and pyrite-quartz veins in the Gaolishan Formation sandstone, and the calculated fluid oxygen isotopic compositions based on fluid inclusion homogenization temperatures in this study. See text for detailed discussion.

Fig.12. Wetherill concordia plots and weighted average $^{206}Pb/^{238}U$ ages of the zircons from the igneous rocks at Xinqiao. A and C are data for the marginal phase quartz diorite from the Jitou stock; B and D are data for the alteration free diorite porphyry distributed in the open pit, see text for details.

Fig.13. Isochron plot showing the pyrite Re-Os data analysed in this study. Also presented are the 320 Ma and 138 Ma reference lines. See text for discussion.

Fig.14. A) Published pyrite sulfur isotopic data of the Carboniferous sedimentary rocks, Cretaceous igneous rocks and associated porphyry-skarn deposits within Middle and Lower Yangtze Metallogenic Belt; B) Published pyrite sulfur isotopic data of the stratabound deposits in Middle and Lower Yangtze Metallogenic Belt, also showing is data from Red Dog deposit. Data are from (Zhou et al. 1983; Liu et al. 1984; Zhou 1984; Zhao et al. 1985; Pan and Dong 1999; Leach et al. 2004; Xu et al. 2004; Li 2006; Xu et al. 2010). See text for discussion.

Fig.15. Published geochronology data of the Cretaceous igneous rocks, associated porphyry-skarn deposits and stratabound massive sulfide deposits in Middle and Lower Yangtze Metallogenic Belt. Data are from (Wu 1996; Wu and Zou 1997; Meng et al. 2004; Wang et al. 2004; Xu et al. 2004; Ding et al. 2005; Wang et al. 2005; Mao et al. 2006; Li et al. 2007; Lu 2007; Wu et al. 2009; Xie et al. 2009; Li et al. 2010b; Guo et al. 2011; Yang et al. 2011a; Yang et al. 2011b). See text for discussion.

Fig.16. Soil Cu, Pb, Zn, Au and Ag geochemical anomaly map for the Tongling mining district (Jiujiang conference communication, 2010, unpublished data).

Table 1. SIMS quartz oxygen isotope data of the skarn ore and pyrite quartz veins in Gaolishan Forma

Sample No.	$\delta^{18}O$ ‰	2σ
quartz from the sakrn ore		
XQ5-1_1	12.85	0.34
XQ5-1_2	11.09	0.18
XQ5-1_3	12.22	0.33
XQ5-1_4	12.80	0.25
XQ5-1_5	13.25	0.34
XQ5-1_6	12.47	0.27
XQ5-1_7	13.69	0.37
XQ5-1_8	12.54	0.37
XQ5-1_9	13.79	0.22
XQ5-1_10	12.02	0.41
XQ5-1_11	12.16	0.25
XQ5-2_1	11.99	0.42
XQ5-2_2	12.25	0.31
XQ5-2_3	11.65	0.38
XQ5-2_4	12.72	0.27
XQ5-2_5	12.23	0.28
XQ5-2_6	12.02	0.35
XQ5-2_7	15.68	0.28
XQ5-2_8	12.17	0.28
XQ5-2_9	14.31	0.40
XQ5-2_10	12.52	0.35
XQ5-3_1	12.22	0.31
XQ5-3_2	16.03	0.30
XQ5-3_3	11.44	0.44
XQ5-3_4	11.79	0.33
XQ5-3_5	13.23	0.35
XQ5-3_6	12.42	0.36
XQ5-3_7	12.50	0.36
XQ5-3_8	11.98	0.35
XQ5-3_9	12.54	0.30
XQ5-3_10	12.28	0.38
XQ5-3_11	12.27	0.26
quartz from vein nettworks in the Gaolishan Formation sandstone		
XQ8-1_1	14.16	0.30
XQ8-1_2	15.21	0.30
XQ8-1_3	14.36	0.49
XQ8-1_4	15.60	0.31
XQ8-1_5	14.40	0.24
XQ8-1_6	15.52	0.31
XQ8-1_7	14.80	0.41
XQ8-1_8	14.92	0.32
XQ8-1_9	14.10	0.29
XQ8-1_10	14.57	0.54
XQ8-1_11	15.44	0.36

XQ8-1_12	15.45	0.31
XQ8-1_13	14.37	0.29
XQ8-2_1	20.28	0.35
XQ8-2_2	17.10	0.21
XQ8-2_3	14.69	0.36
XQ8-2_4	16.07	0.18
XQ8-2_5	16.74	0.33
XQ8-2_6	14.44	0.26
XQ8-2_7	15.24	0.34
XQ8-2_8	17.21	0.28
XQ8-2_9	19.93	0.35
XQ8-2_10	13.47	0.50
XQ8-2_11	15.08	0.41
XQ8-2_12	19.06	0.35
XQ8-2_13	15.90	0.31
XQ8-3_1	15.03	0.26
XQ8-3_2	16.86	0.37
XQ8-3_3	16.57	0.31
XQ8-3_4	14.89	0.45
XQ8-3_5	15.99	0.38
XQ8-3_6	15.55	0.28
XQ8-3_7	15.85	0.32
XQ8-3_8	16.00	0.44
XQ8-3_9	15.89	0.43
XQ8-3_10	15.68	0.28
XQ8-4_1	16.55	0.27
XQ8-4_2	16.35	0.38
XQ8-4_3	19.30	0.38
XQ8-4_4	14.77	0.26
XQ8-4_5	15.33	0.86
XQ8-4_6	10.16	0.40
XQ8-4_7	10.51	0.30
XQ8-4_8	16.94	0.24
XQ8-4_9	17.13	0.28
XQ8-5_1	14.51	0.22
XQ8-5_2	12.53	0.38
XQ8-5_3	17.07	0.38
XQ8-5_4	16.27	0.33
XQ8-5_5	16.82	0.24
XQ8-5_6	13.73	0.30
XQ8-5_7	16.31	0.22
XQ8-5_8	17.09	0.33
XQ8-5_9	13.72	0.28
XQ8-5_10	17.76	0.32
XQ8-5_11	15.62	0.47
XQ8-5_12	16.43	0.21
XQ8-5_13	12.22	0.33
XQ8-5_14	15.27	0.45

XQ8-6_1	16.43	0.27
XQ8-6_2	15.43	0.37
XQ8-6_3	16.26	0.35
XQ8-6_4	15.54	0.42
XQ8-6_5	15.26	0.46
XQ8-6_6	17.67	0.39
XQ8-6_7	13.87	0.36
XQ8-6_8	15.89	0.34
XQ8-6_9	16.15	0.31
XQ8-6_10	15.39	0.40
XQ8-6_11	16.48	0.39
XQ8-6_12	13.70	0.48

Table 2. SIMS zircon U-Pb data of the quartz diorite and diorite porphyry samples at Xinqiao.

Sample No.	U ppm	Th ppm	Th/U	$f^{206}Pb$ %	$^{207}Pb/^{206}Pb$	±1σ %	$^{207}Pb/^{235}U$	±1σ %
Central phase quartz diorite of the Jitou pluton								
XQ09-3@01	232	242	1.04	0.3	0.04939	3.22	0.14156	3.95
XQ09-3@02	99	54	0.54	1.1	0.04734	4.04	0.13985	4.34
XQ09-3@03	209	152	0.73	0.2	0.05104	2.68	0.14676	3.74
XQ09-3@04	109	99	0.91	0.8	0.04984	3.77	0.14904	4.17
XQ09-3@07	167	114	0.68	0.4	0.04943	3.04	0.13937	4.78
XQ09-3@08	261	206	0.79	0.3	0.05228	2.39	0.14985	3.88
XQ09-3@10	214	206	0.97	0.1	0.05260	2.64	0.15443	3.29
XQ09-3@12	175	68	0.39	0.2	0.04899	3.02	0.14864	3.40
XQ09-3@13	114	77	0.67	0.9	0.05100	4.15	0.15218	4.44
XQ09-3@14	186	143	0.77	0.3	0.04988	2.89	0.14933	3.28
XQ09-3@15	204	167	0.82	0.3	0.04893	3.08	0.14906	3.44
XQ09-3@16	151	111	0.73	0.6	0.05235	3.13	0.14291	5.40
XQ09-3@17	132	105	0.79	0.4	0.04929	4.22	0.14847	4.50
XQ09-3@18	300	301	1.00	0.5	0.05160	2.27	0.14176	4.16
XQ09-3@19	171	128	0.75	0.0	0.05025	3.04	0.14918	3.40
XQ09-3@20	203	216	1.07	0.3	0.04851	2.84	0.14487	3.24
Post-ore diorite porphyry								
XQ-1@01	466	213	0.46	0.2	0.04745	1.35	0.13398	2.03
XQ-1@02	794	365	0.46	0.1	0.04820	1.29	0.13562	2.05
XQ-1@03	807	452	0.56	0.1	0.04838	1.08	0.13763	1.85
XQ-1@04	810	359	0.44	0.1	0.04746	0.94	0.13325	1.81
XQ-1@05	810	504	0.62	0.0	0.04897	1.00	0.14153	1.80
XQ-1@06	294	149	0.51	0.1	0.04919	1.50	0.13965	2.15
XQ-1@07	993	541	0.55	0.1	0.04935	0.69	0.14218	1.66
XQ-1@09	510	196	0.38	0.2	0.04768	1.59	0.13462	2.19
XQ-1@10	467	217	0.47	0.2	0.04806	1.75	0.13267	2.32
XQ-1@11	811	411	0.51	0.1	0.04928	1.04	0.13754	1.82
XQ-1@12	472	335	0.71	0.3	0.04687	1.58	0.12993	2.19
XQ-1@14	764	453	0.59	0.2	0.04779	1.12	0.13309	1.93
XQ-1@15	417	269	0.65	0.1	0.04848	1.23	0.14168	1.94
XQ-1@16	474	190	0.40	0.1	0.04928	1.08	0.14057	1.87
XQ-1@17	609	291	0.48	0.1	0.04949	0.91	0.13951	1.77
XQ-1@18	571	252	0.44	0.1	0.04903	0.91	0.14170	1.80
XQ-1@19	448	264	0.59	0.2	0.04770	1.41	0.13468	2.13
XQ-1@20	446	247	0.55	0.2	0.04686	1.53	0.13286	2.14
XQ-1@22	837	482	0.58	0.1	0.04858	0.82	0.13501	1.77
XQ-1@23	405	261	0.64	0.1	0.04982	1.39	0.13937	2.06
XQ-1@25	902	496	0.55	0.2	0.04811	1.70	0.13697	2.28
XQ-1@26	468	204	0.43	0.1	0.05021	1.51	0.13795	2.14

$^{206}Pb/^{238}U$	±1σ	rho	$t^{207}Pb/^{235}U$	±1σ	$t^{206}Pb/^{238}U$	±1σ
	%		Ma	abs	Ma	abs
0.02167	1.51	0.38	134.4	5.0	138.2	2.1
0.02142	1.59	0.37	132.9	5.4	136.6	2.1
0.02167	1.55	0.42	139.0	4.9	138.2	2.1
0.02169	1.77	0.43	141.1	5.5	138.3	2.4
0.02173	1.53	0.32	132.5	6.0	138.6	2.1
0.02178	1.50	0.39	141.8	5.1	138.9	2.1
0.02165	1.51	0.46	145.8	4.5	138.0	2.1
0.02200	1.55	0.46	140.7	4.5	140.3	2.2
0.02164	1.59	0.36	143.8	6.0	138.0	2.2
0.02171	1.56	0.47	141.3	4.3	138.5	2.1
0.02209	1.53	0.44	141.1	4.5	140.9	2.1
0.02181	1.58	0.29	135.6	6.9	139.1	2.2
0.02184	1.58	0.35	140.6	5.9	139.3	2.2
0.02155	1.51	0.36	134.6	5.3	137.5	2.1
0.02153	1.52	0.45	141.2	4.5	137.3	2.1
0.02166	1.55	0.48	137.4	4.2	138.2	2.1
0.02048	1.53	0.75	127.7	2.4	130.7	2.0
0.02041	1.60	0.78	129.1	2.5	130.2	2.1
0.02063	1.50	0.81	130.9	2.3	131.6	2.0
0.02036	1.55	0.86	127.0	2.2	129.9	2.0
0.02096	1.50	0.83	134.4	2.3	133.7	2.0
0.02059	1.54	0.72	132.7	2.7	131.4	2.0
0.02089	1.51	0.91	135.0	2.1	133.3	2.0
0.02048	1.51	0.69	128.2	2.6	130.7	2.0
0.02002	1.52	0.66	126.5	2.8	127.8	1.9
0.02024	1.50	0.82	130.8	2.2	129.2	1.9
0.02011	1.52	0.69	124.0	2.6	128.3	1.9
0.02020	1.57	0.81	126.9	2.3	128.9	2.0
0.02119	1.50	0.77	134.5	2.4	135.2	2.0
0.02069	1.53	0.82	133.5	2.3	132.0	2.0
0.02044	1.52	0.86	132.6	2.2	130.5	2.0
0.02096	1.55	0.86	134.6	2.3	133.7	2.1
0.02048	1.60	0.75	128.3	2.6	130.7	2.1
0.02056	1.50	0.70	126.7	2.6	131.2	2.0
0.02015	1.57	0.89	128.6	2.1	128.6	2.0
0.02029	1.52	0.74	132.5	2.6	129.5	1.9
0.02065	1.52	0.67	130.3	2.8	131.8	2.0
0.01993	1.51	0.71	131.2	2.6	127.2	1.9

Table 3. Pyrite Re-Os data of the stratabound massive orebody at Xinqiao.

Sample No.	Re	±	Os	±	^{192}Os	±	$^{187}Re/^{188}Os$	±	$^{187}Os/^{188}Os$
	ppb		ppt		ppt				
XQ15*	1.10	0.01	31.8	0.4	11.0	0.3	198.1	5.8	1.60
XQ24	31.88	0.12	124.7	2.2	26.0	0.6	2439.5	57.3	7.64
XQ25	28.87	0.11	64.3	4.1	9.0	0.6	6377.7	420.8	15.07
XQ10	26.05	0.10	50.9	7.0	3.9	0.4	14870.1	1715.6	38.70

±	rho	initial $^{187}Os/^{188}Os$ @320 Ma	±	initial $^{187}Os/^{188}Os$ @138 Ma	±
0.05	0.925	0.5	0.1	1.1	0.1
0.18	0.985	-5.4	0.5	2.0	0.3
0.99	0.997	-18.9	3.2	0.4	1.9
4.46	0.999	-40.6	13.4	4.5	8.3

Table 4. Geochronology data for stratiform massive sulfide deposits and Meosozoic intrusions and deposits a

Deposit	Sample type	Age/Ma	Method
Wushan	Granodiorite-porphyry	148.0±1.0	LA-ICP-MS Zircon U-Pb
	Granodiorite-porphyry	147.3±0.9	LA-ICP-MS Zircon U-Pb
	Granodiorite-porphyry	145.4±0.9	LA-ICP-MS Zircon U-Pb
	Lamprophyre	144.3±0.9	LA-ICP-MS Zircon U-Pb
	Lamprophyre	143.6±0.9	LA-ICP-MS Zircon U-Pb
	Mafic dike	144.5±1.2	LA-ICP-MS Zircon U-Pb
	Mafic dike	142.6±1.0	LA-ICP-MS Zircon U-Pb
	Granodiorite-porphyry	146.6±1.0	SIMS Zircon U-Pb
	Granodiorite-porphyry	146.2±1.2	SIMS Zircon U-Pb
	Granodiorite-porphyry	144.6±3.9	SIMS Zircon U-Pb
	Skarn orebody	146.4±2.6	Molybdenite Re-Os
Chengmenshan	Granodiorite-porphyry	144.5±1.3	SIMS Zircon U-Pb
	Porphyry Cu	137.0±3	Molybdenite Re-Os
	Porphyry Cu	141.0±3	Molybdenite Re-Os
	Porphyry Cu	142.3±2.3	Molybdenite Re-Os
Dongguashan	Quartz monzodiorite	138.8±1.6	LA-ICP-MS Zircon U-Pb
	Quartz monzodiorite	135.6±1.4	Whole rock Rb-Sr
	Pyroxene monzonite	148.2±3.1	SHRIMP Zircon U-Pb
	Quartz monzodiorite	135.5±2.2	SHRIMP Zircon U-Pb
	Quartz monzodiorite	135.8±1.1	Biotite Ar-Ar
	Porphyry-Skarn Cu	137.4(?)	Pyrite Re-Os model age
Xinqiao	Monzodiorite	146.4±4.3	SHRIMP Zircon U-Pb
	Quartz monzodiorite	140.4±2.2	SHRIMP Zircon U-Pb
	Pyrite vein in sandstone	319±13	Pyrite Re-Os isochron
	Stratiform orebody	112.6±7.8	Pyrite Rb-Sr isochron
	Stratiform orebody	126±11	Pyrite Re-Os isochron
Simenkou	Stratiform orebody	303±33	Pyrite Re-Os isochron
Jinkouyu	Stratiform orebody	137±0.19	Pyrite Re-Os isochron

along MLYMB

References
(Ding et al., 2005; Yang et al., 2011a)
(Li et al., 2010c)
(Li et al., 2007)
(Li et al., 2010c)
(Wu and Zou, 1997)
(Mao et al., 2006)
(Yang et al., 2011b) (Xu et al., 2004b) (Wu et al., 2009) (Lu, 2007) (Wu, 1996) (Meng et al., 2004)
(Wu et al., 2009)
(Guo et al., 2011) (Wang et al., 2005) (Xie et al., 2009)
(Meng et al., 2004)

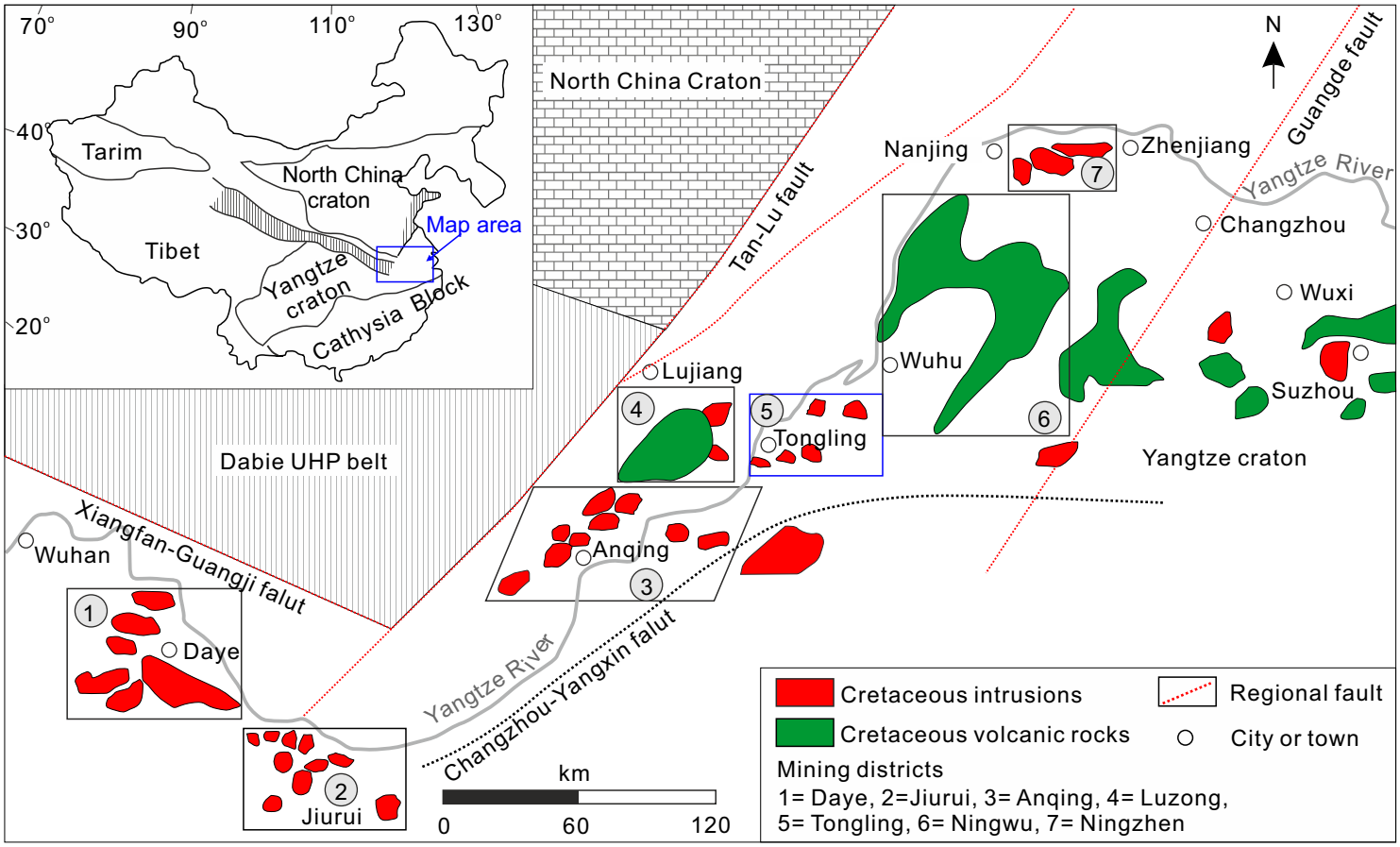
70°
90°
110°
130°
40°
30°
20°
Tarim
North China craton
Tibet
Yangtze craton
Cathysia Block
Map area
North China Craton
Tan-Lu fault
Guangde fault
N
Nanjing
Zhenjiang
Yangtze River
Changzhou
Wuxi
Suzhou
Wuhu
Lujiang
Tongling
Anqing
Yangtze craton
Dabie UHP belt
Xiangfan-Guangji falut
Wuhan
Daye
Jiurui
Changzhou-Yangxin falut
km
0
60
120
Cretaceous intrusions
Cretaceous volcanic rocks
Regional fault
City or town
Mining districts
1= Daye, 2=Jiurui, 3= Anqing, 4= Luzong,
5= Tongling, 6= Ningwu, 7= Ningzhen

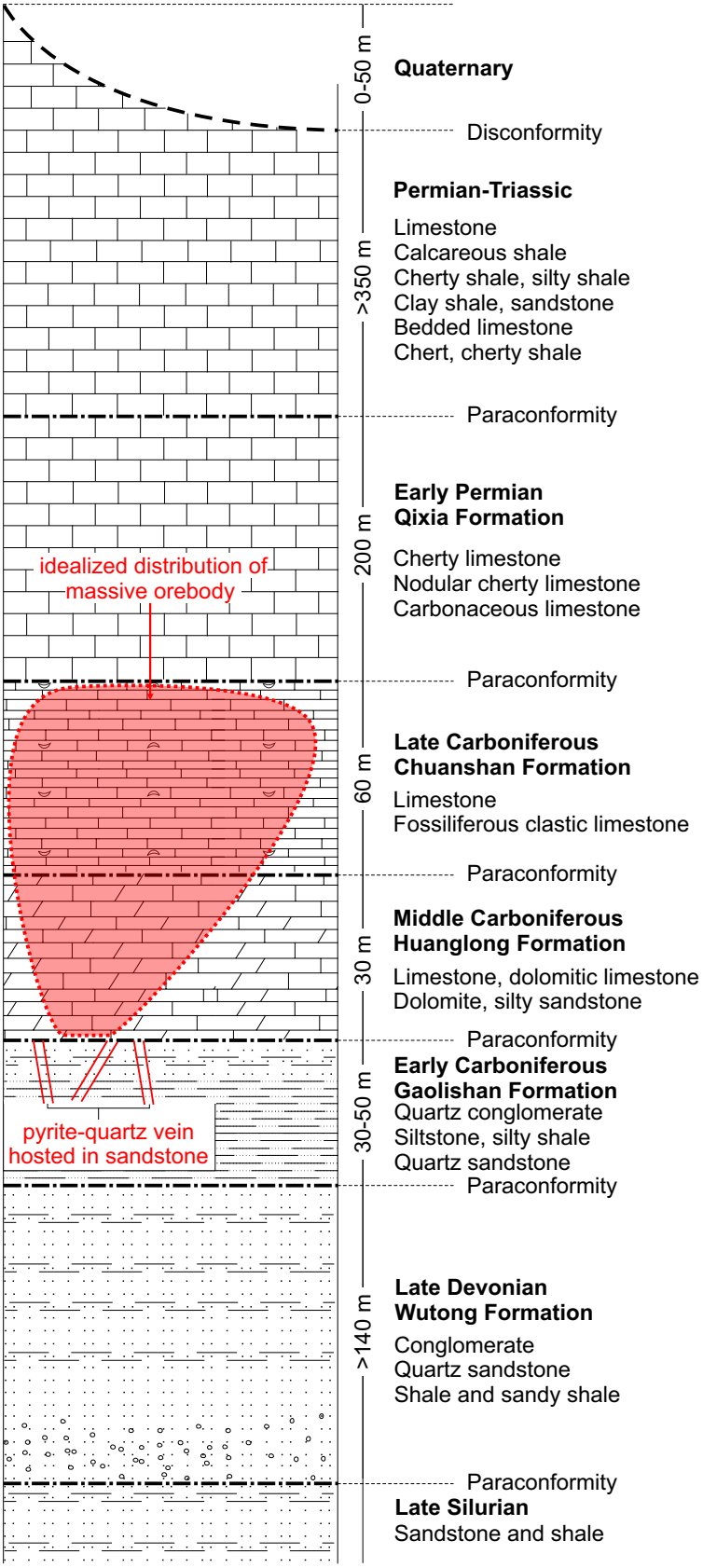
0-50 m
Quaternary
Disconformity
Permian-Triassic
Limestone
Calcareous shale
Cherty shale, silty shale
Clay shale, sandstone
Bedded limestone
Chert, cherty shale
>350 m
Paraconformity
Early Permian
Qixia Formation
Cherty limestone
Nodular cherty limestone
Carbonaceous limestone
200 m
idealized distribution of
massive orebody
Paraconformity
Late Carboniferous
Chuanshan Formation
Limestone
Fossiliferous clastic limestone
60 m
Paraconformity
Middle Carboniferous
Huanglong Formation
Limestone, dolomitic limestone
Dolomite, silty sandstone
30 m
Paraconformity
Early Carboniferous
Gaolishan Formation
Quartz conglomerate
Siltstone, silty shale
Quartz sandstone
30-50 m
pyrite-quartz vein
hosted in sandstone
Paraconformity
Late Devonian
Wutong Formation
Conglomerate
Quartz sandstone
Shale and sandy shale
>140 m
Paraconformity
Late Silurian
Sandstone and shale

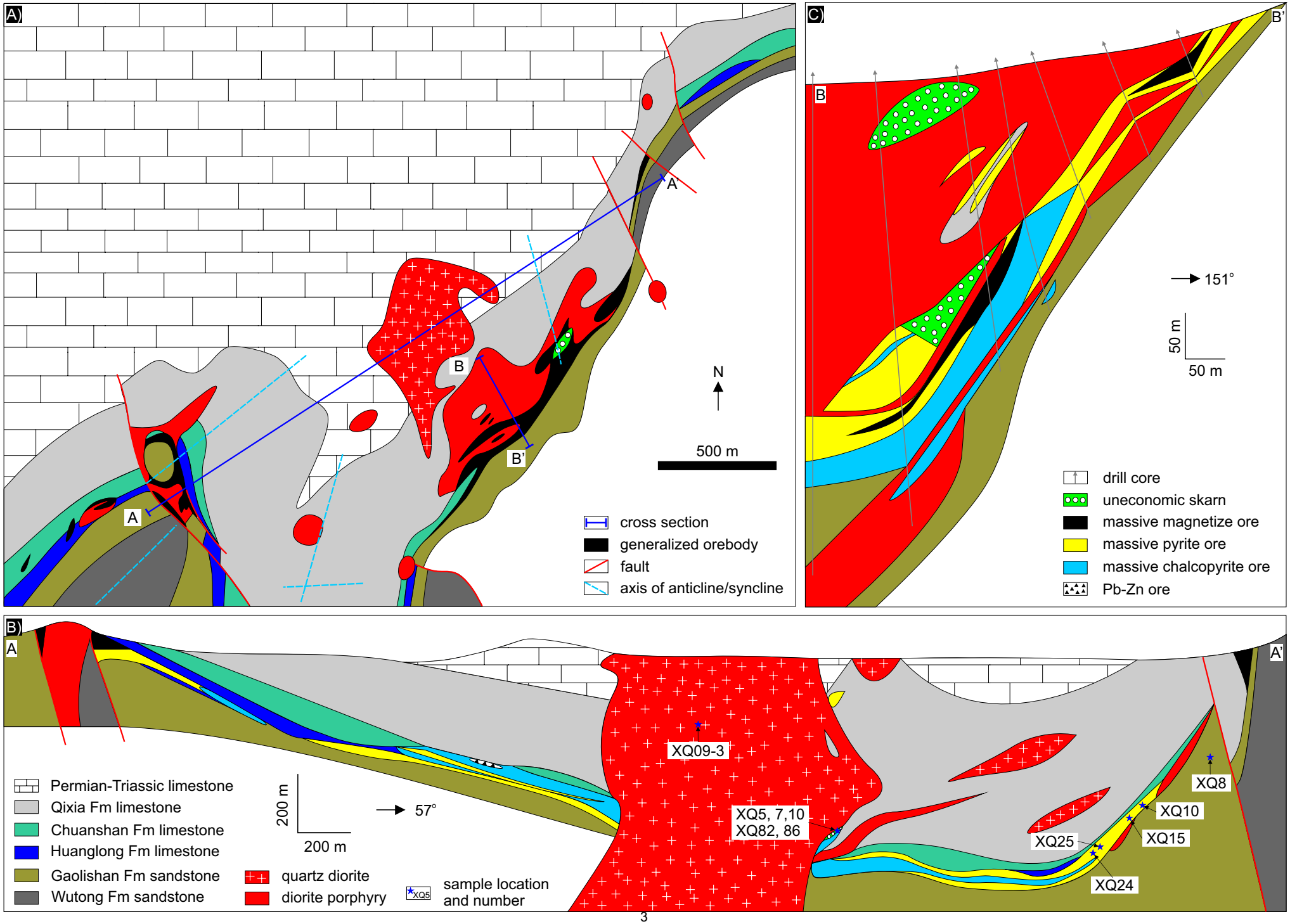
A)
A
A'
B
B'
N
500 m
cross section
generalized orebody
fault
axis of anticline/syncline
C)
B
B'
151°
50 m
50 m
drill core
uneconomic skarn
massive magnetize ore
massive pyrite ore
massive chalcopyrite ore
Pb-Zn ore
B)
A
A'
XQ09-3
XQ5, 7,10
XQ82, 86
XQ8
XQ10
XQ15
XQ25
XQ24
200 m
200 m
57°
Permian-Triassic limestone
Qixia Fm limestone
Chuanshan Fm limestone
Huanglong Fm limestone
Gaolishan Fm sandstone
Wutong Fm sandstone
quartz diorite
diorite porphyry
XQ5
sample location and number

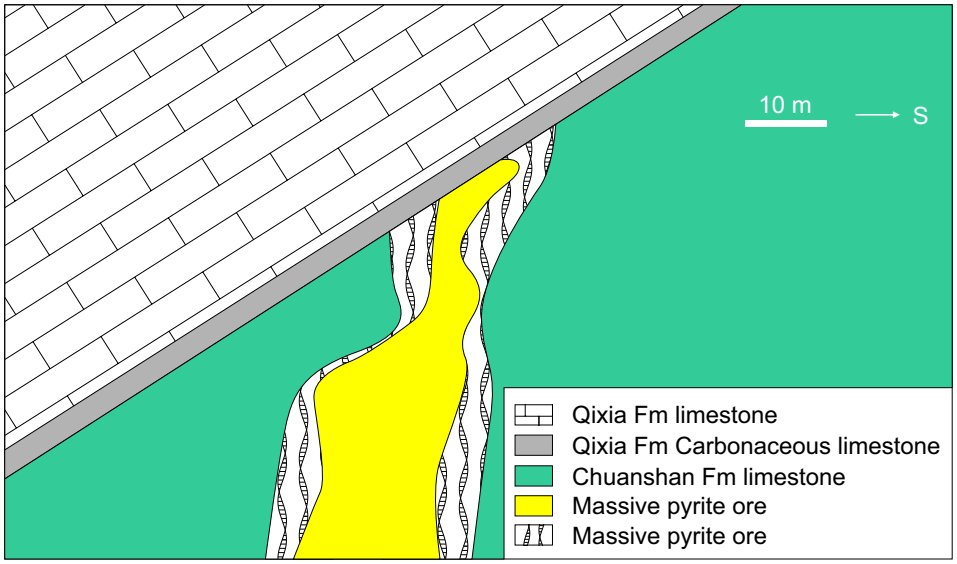
10 m
S
Qixia Fm limestone
Qixia Fm Carbonaceous limestone
Chuanshan Fm limestone
Massive pyrite ore
Massive pyrite ore

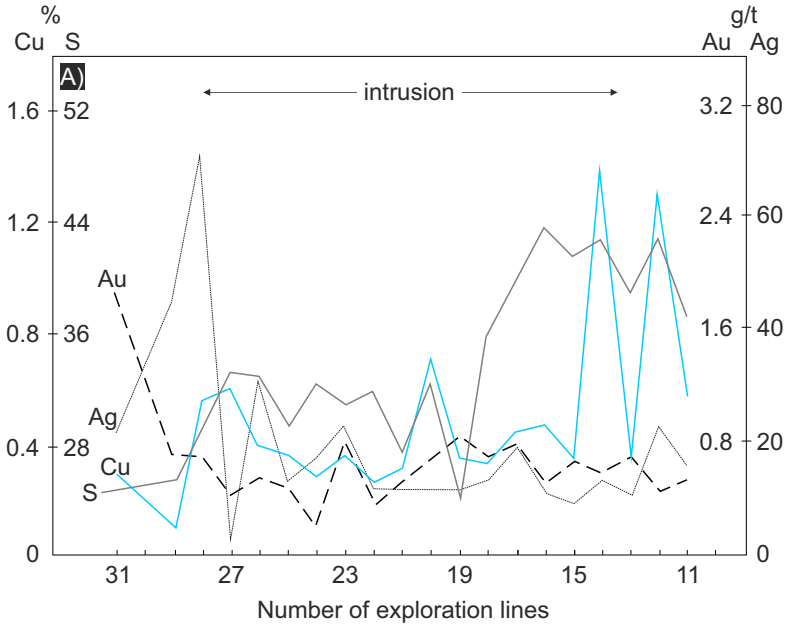
%
Cu S
g/t
Au Ag
A)
intrusion
1.6 52
1.2 44
0.8 36
0.4 28
0
3.2 80
2.4 60
1.6 40
0.8 20
0
Au
Ag
Cu
S
31 27 23 19 15 11
Number of exploration lines

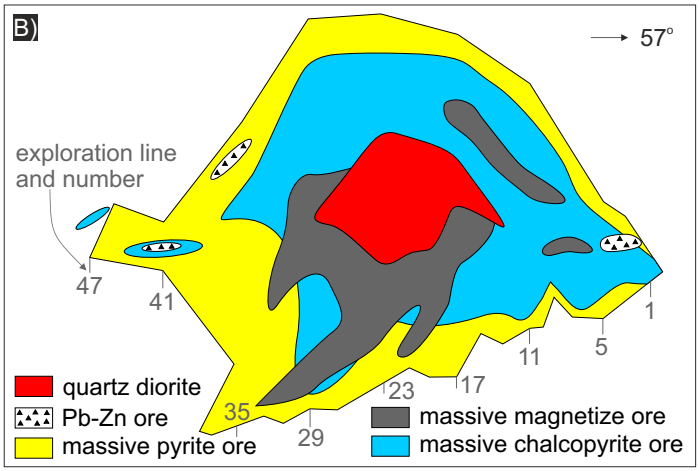
B)
57°
exploration line
and number
47
41
35
29
23
17
11
5
1
quartz diorite
Pb-Zn ore
massive pyrite ore
massive magnetize ore
massive chalcopyrite ore

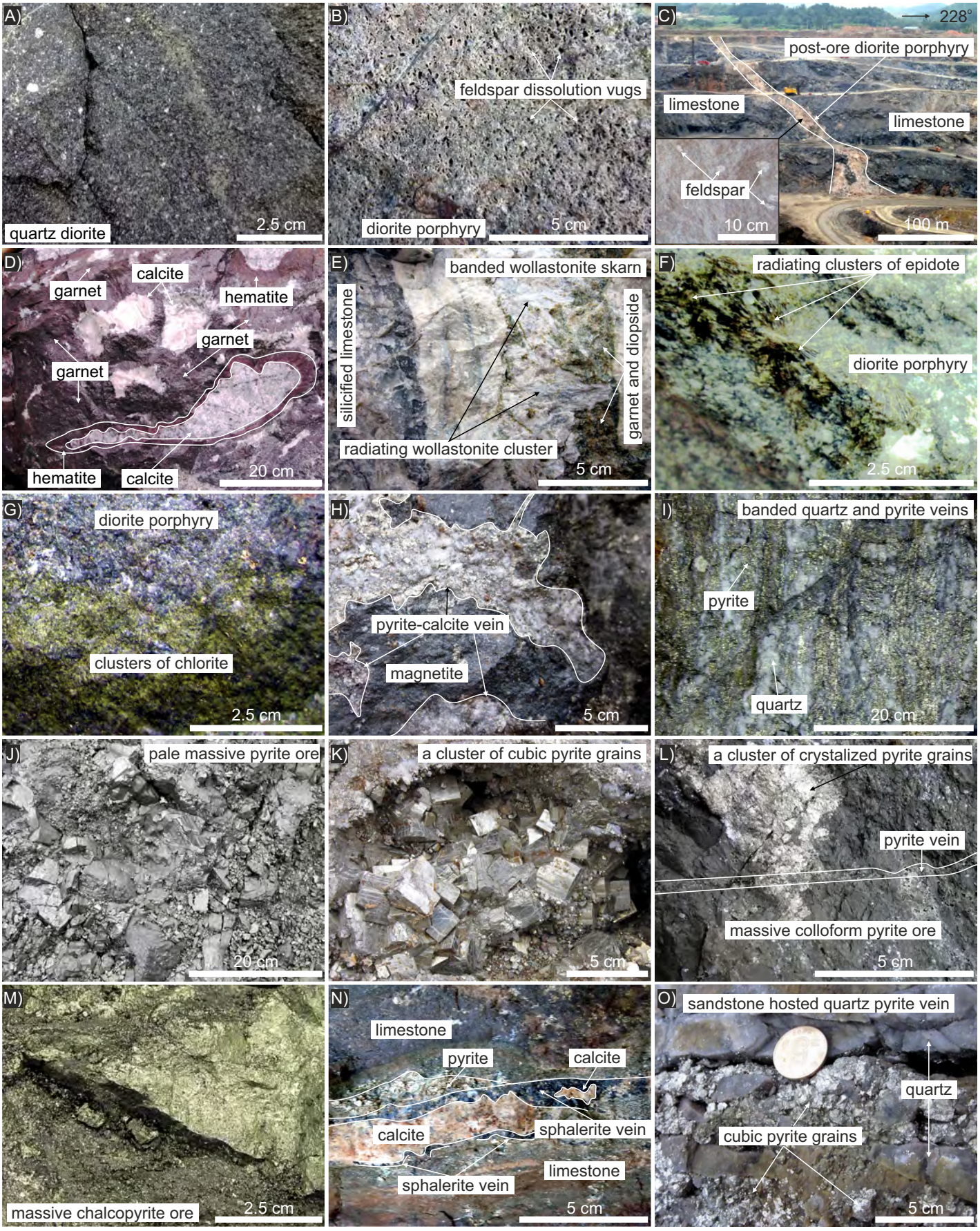
A)
quartz diorite
2.5 cm
B)
feldspar dissolution vugs
diorite porphyry
5 cm
C)
228°
post-ore diorite porphyry
limestone
limestone
feldspar
10 cm
100 m
D)
garnet
calcite
hematite
garnet
garnet
hematite
calcite
20 cm
E)
banded wollastonite skarn
silicified limestone
garnet and diopside
radiating wollastonite cluster
5 cm
F)
radiating clusters of epidote
diorite porphyry
2.5 cm
G)
diorite porphyry
clusters of chlorite
2.5 cm
H)
pyrite-calcite vein
magnetite
5 cm
I)
banded quartz and pyrite veins
pyrite
quartz
20 cm
J)
pale massive pyrite ore
20 cm
K)
a cluster of cubic pyrite grains
5 cm
L)
a cluster of crystalized pyrite grains
pyrite vein
massive colloform pyrite ore
5 cm
M)
massive chalcopyrite ore
2.5 cm
N)
limestone
pyrite
calcite
calcite
sphalerite vein
limestone
sphalerite vein
5 cm
O)
sandstone hosted quartz pyrite vein
quartz
cubic pyrite grains
5 cm

minerals	uneconomic skarn	mineralization stage
garnet		
diopside		
wollastonite		
epidote		
tremolite		
chlorite		
magnetite		
hematite		
sericite		
calcite		
quartz		
pyrite		
colloform pyrite		
chalcopyrite		
sphalerite		
galena		

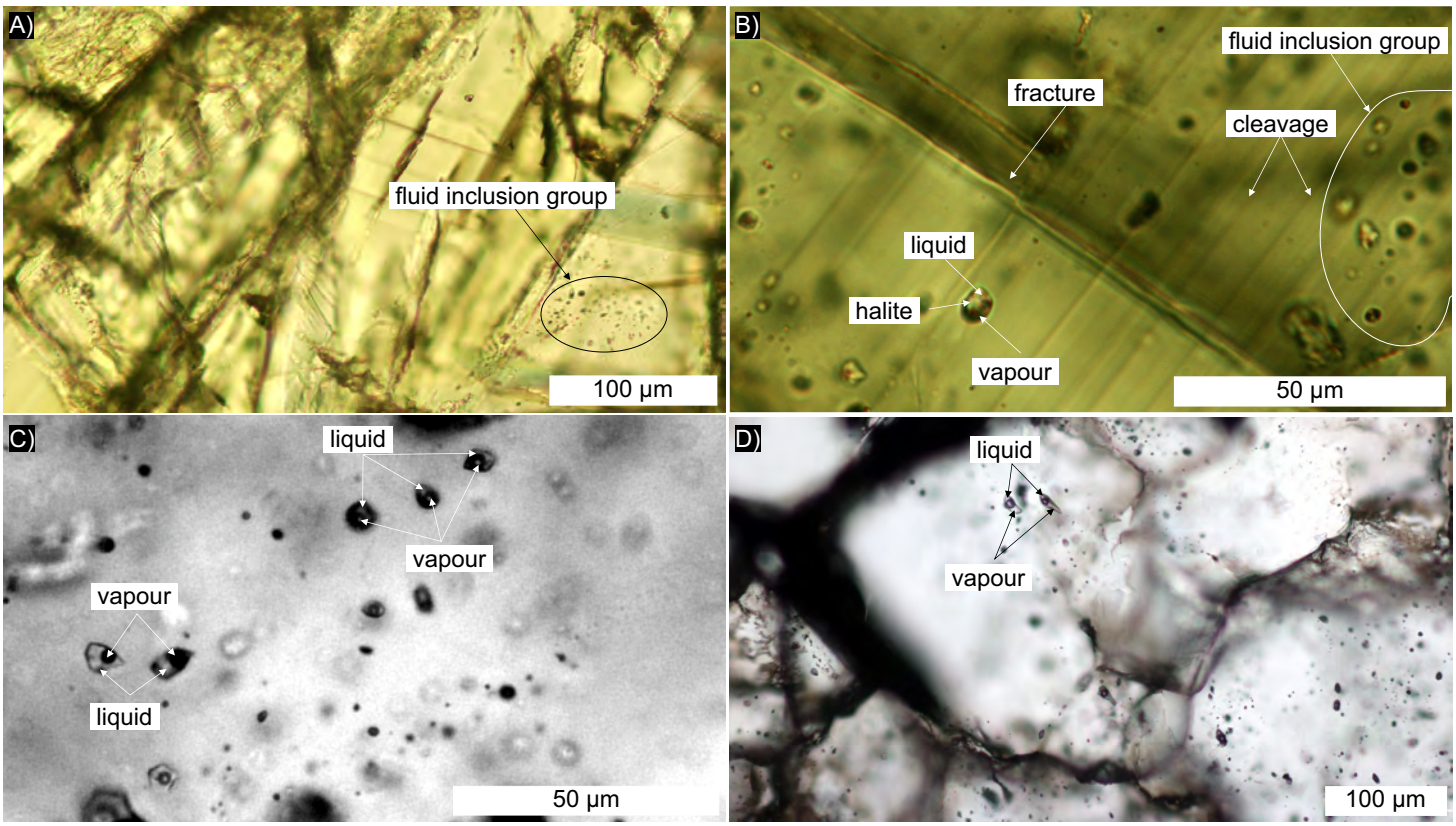
A)
fluid inclusion group
100 µm
B)
fluid inclusion group
fracture
cleavage
liquid
halite
vapour
50 µm
C)
liquid
vapour
vapour
liquid
50 µm
D)
liquid
vapour
100 µm

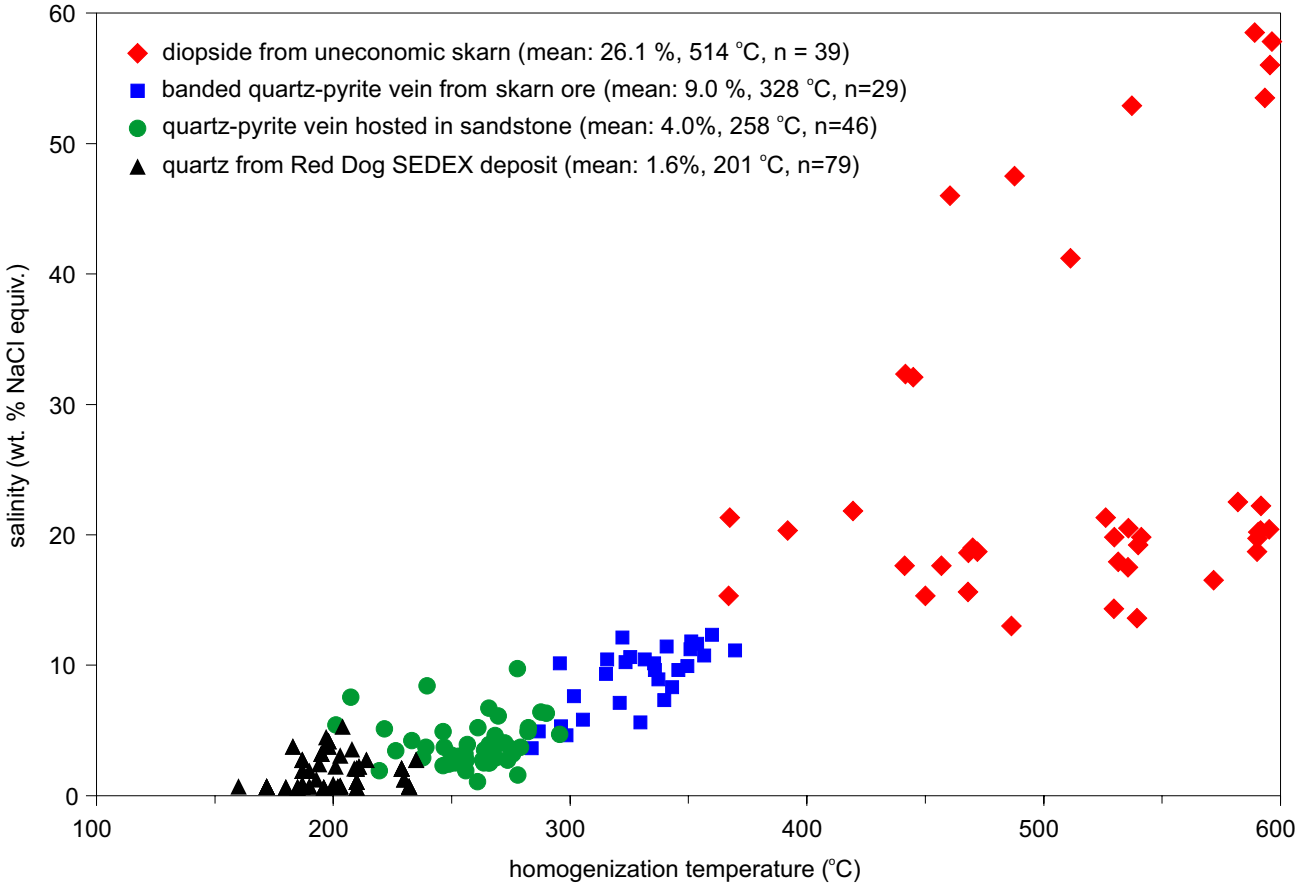
diopside from uneconomic skarn (mean: 26.1 %, 514 ˚C, n = 39)
banded quartz-pyrite vein from skarn ore (mean: 9.0 %, 328 ˚C, n=29)
quartz-pyrite vein hosted in sandstone (mean: 4.0%, 258 ˚C, n=46)
quartz from Red Dog SEDEX deposit (mean: 1.6%, 201 ˚C, n=79)
salinity (wt. % NaCl equiv.)
homogenization temperature (˚C)
0
10
20
30
40
50
60
100
200
300
400
500
600

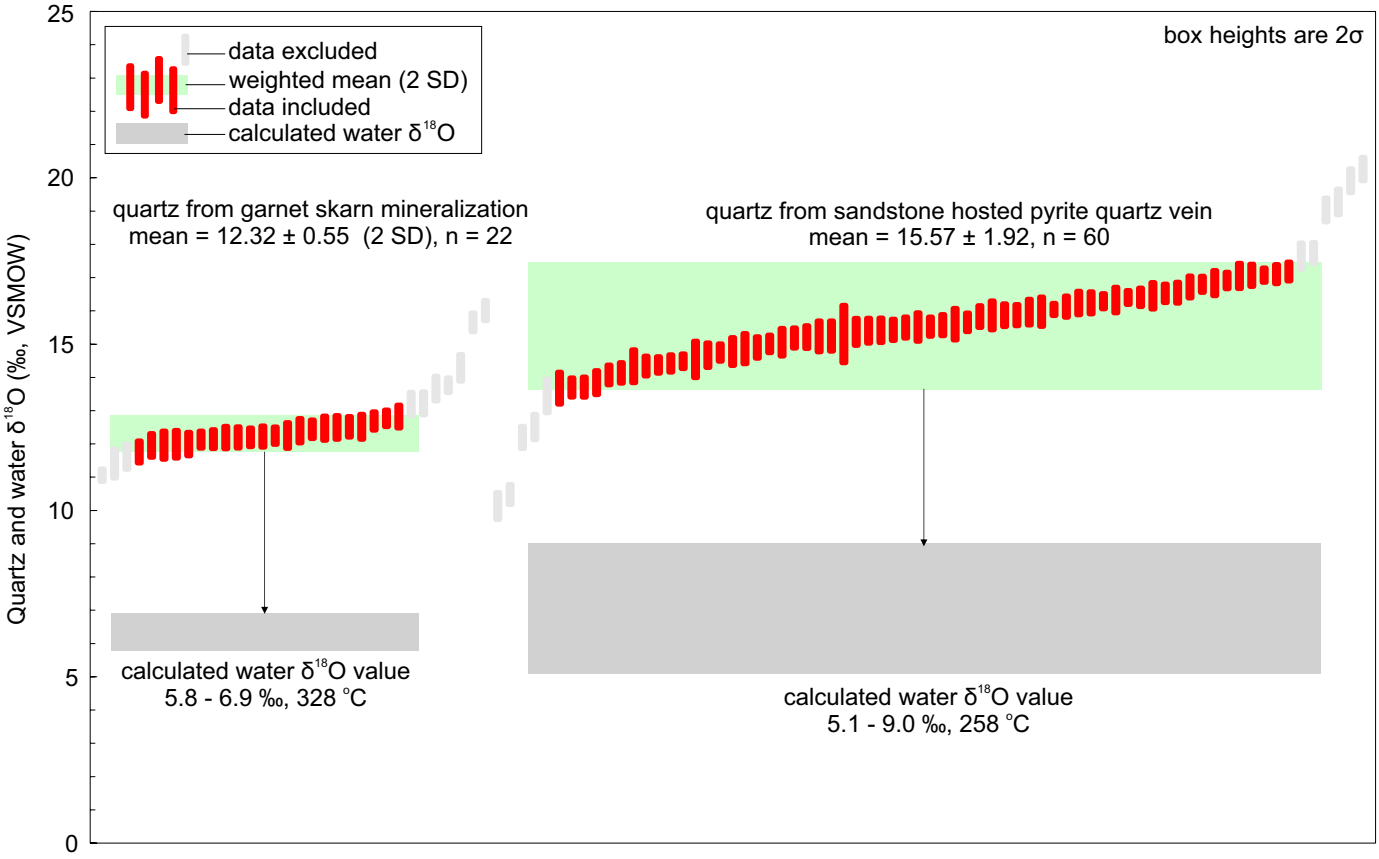
box heights are 2σ
data excluded
weighted mean (2 SD)
data included
calculated water δ18O
quartz from garnet skarn mineralization
mean = 12.32 ± 0.55 (2 SD), n = 22
quartz from sandstone hosted pyrite quartz vein
mean = 15.57 ± 1.92, n = 60
calculated water δ18O value
5.8 - 6.9 ‰, 328 °C
calculated water δ18O value
5.1 - 9.0 ‰, 258 °C
Quartz and water δ18O (‰, VSMOW)
25
20
15
10
5
0

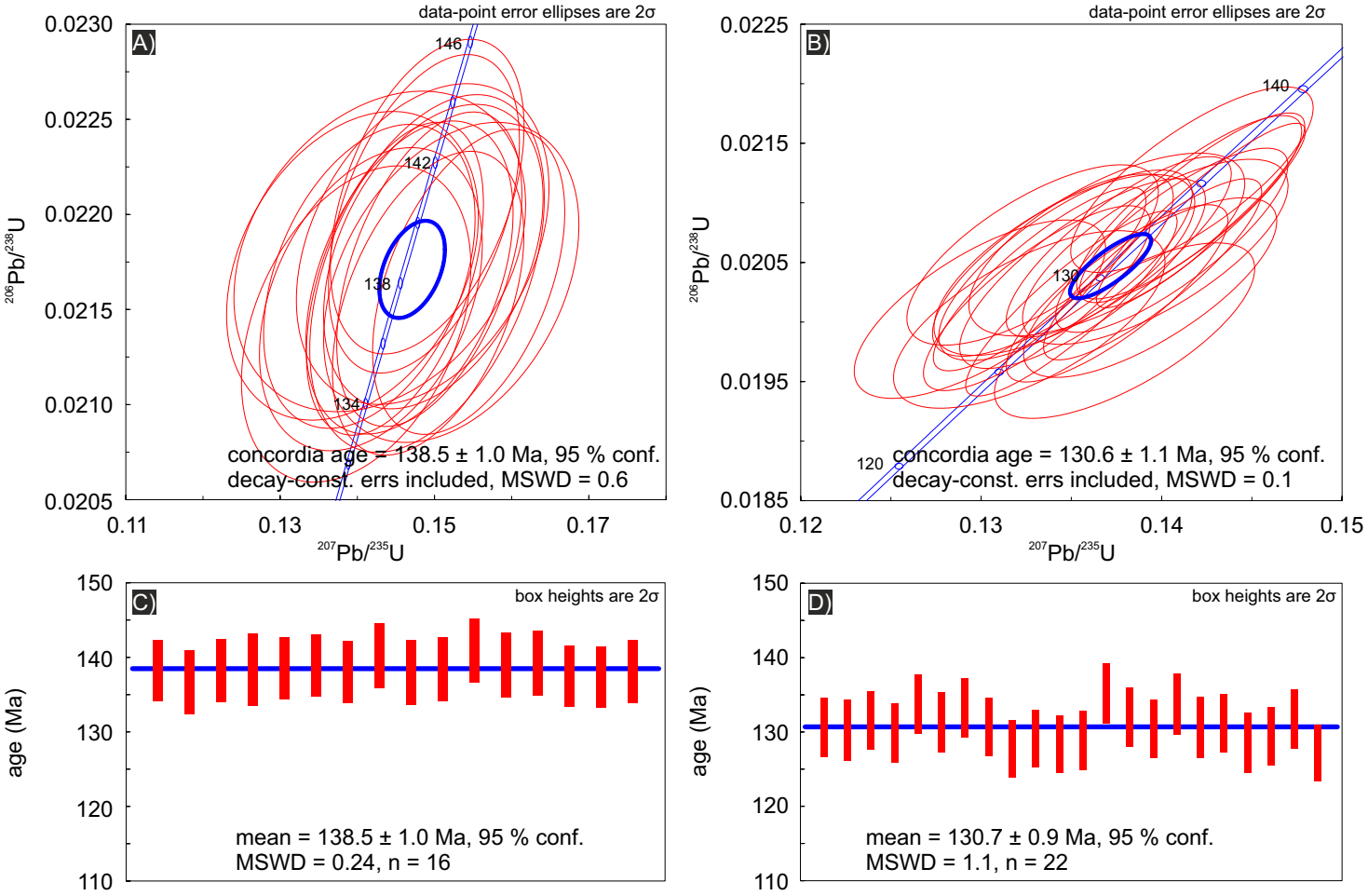
A)
data-point error ellipses are 2σ
146
142
138
134
concordia age = 138.5 ± 1.0 Ma, 95 % conf.
decay-const. errs included, MSWD = 0.6
$^{206}Pb/^{238}U$
$^{207}Pb/^{235}U$
B)
data-point error ellipses are 2σ
140
130
120
concordia age = 130.6 ± 1.1 Ma, 95 % conf.
decay-const. errs included, MSWD = 0.1
C)
box heights are 2σ
mean = 138.5 ± 1.0 Ma, 95 % conf.
MSWD = 0.24, n = 16
age (Ma)
D)
box heights are 2σ
mean = 130.7 ± 0.9 Ma, 95 % conf.
MSWD = 1.1, n = 22

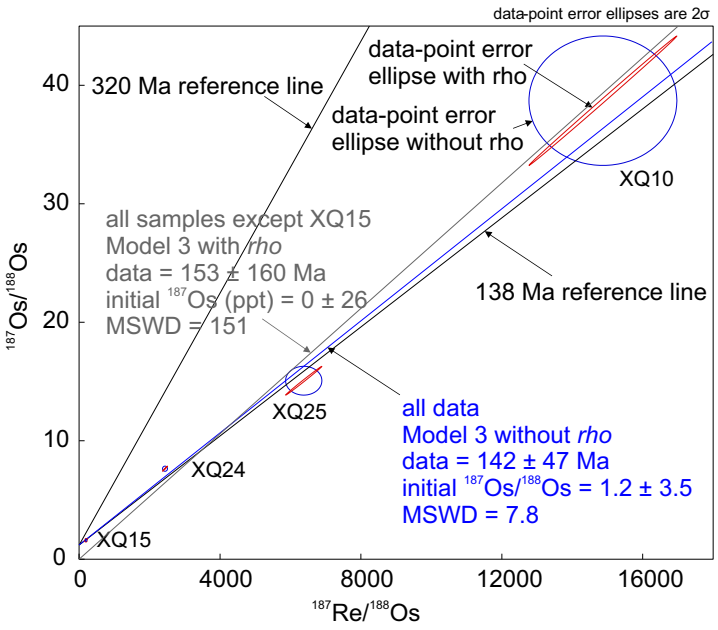
data-point error ellipses are 2σ
data-point error ellipse with rho
data-point error ellipse without rho
320 Ma reference line
XQ10
all samples except XQ15
Model 3 with rho
data = 153 ± 160 Ma
initial 187Os (ppt) = 0 ± 26
MSWD = 151
138 Ma reference line
XQ25
all data
Model 3 without rho
data = 142 ± 47 Ma
initial 187Os/188Os = 1.2 ± 3.5
MSWD = 7.8
XQ24
XQ15
0
10
20
30
40
0
4000
8000
12000
16000
187Os/188Os
187Re/188Os

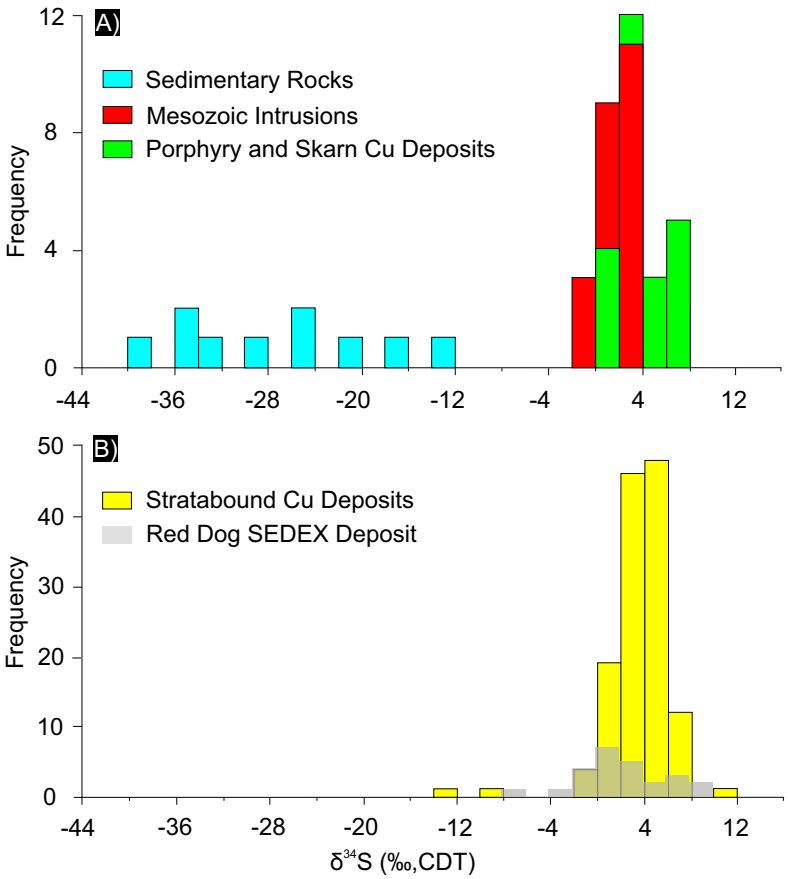
A)
Sedimentary Rocks
Mesozoic Intrusions
Porphyry and Skarn Cu Deposits
Frequency
12
8
4
0
-44
-36
-28
-20
-12
-4
4
12
B)
Stratabound Cu Deposits
Red Dog SEDEX Deposit
Frequency
50
40
30
20
10
0
-44
-36
-28
-20
-12
-4
4
12
δ34S (‰,CDT)

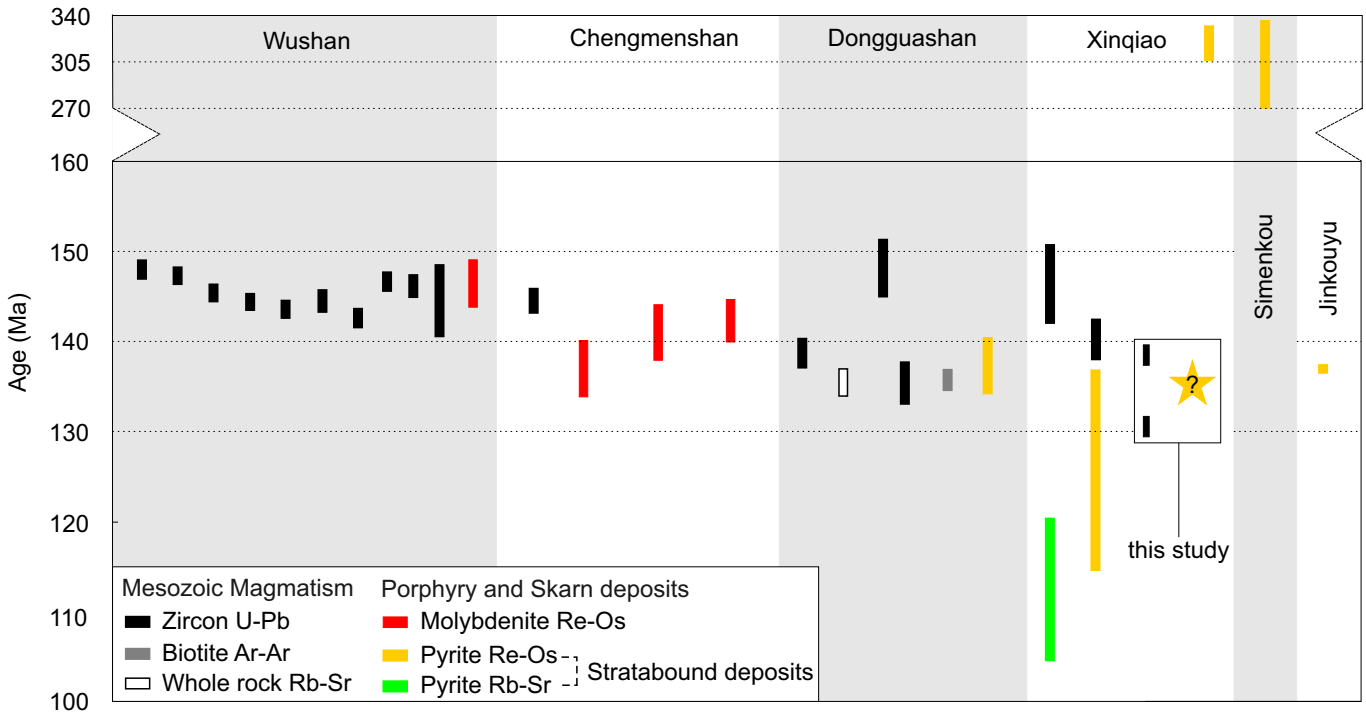
Age (Ma)
340
305
270
160
150
140
130
120
110
100
Wushan
Chengmenshan
Dongguashan
Xinqiao
Simenkou
Jinkouyu
?
this study
Mesozoic Magmatism
Zircon U-Pb
Biotite Ar-Ar
Whole rock Rb-Sr
Porphyry and Skarn deposits
Molybdenite Re-Os
Pyrite Re-Os
Pyrite Rb-Sr
Stratabound deposits

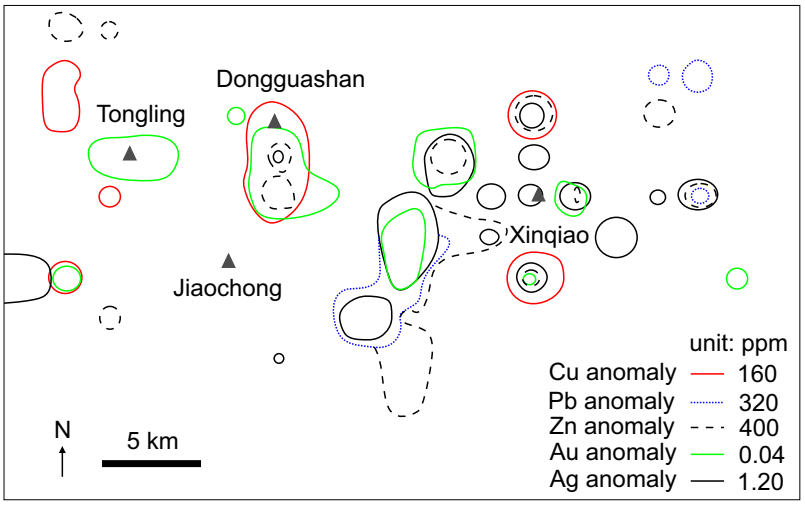
Dongguashan
Tongling
Xinqiao
Jiaochong
N
5 km
unit: ppm
Cu anomaly 160
Pb anomaly 320
Zn anomaly 400
Au anomaly 0.04
Ag anomaly 1.20